Spin transport and current induced magnetization dynamics in magnetic nanostructures.

A DISSERTATION

SUBMITTED TO THE FACULTY OF THE GRADUATE SCHOOL

OF THE UNIVERSITY OF MINNESOTA

BY

Xi Chen

IN PARTIAL FULFILLMENT OF THE REQUIREMENTS

FOR THE DEGREE OF

DOCTOR OF PHILOSOPHY

Randall H. Victora, Adviser

October, 2010

To mom and dad

Abstract

The study of the interaction between conducting electrons and magnetization in a ferromagnet has stimulated much interest following the discovery of the giant magnetoresistive effect two decades ago. With the advance of fabrication techniques at the nanometer length scale, a variety of new magnetic nanostructures have emerged. These structures are interesting from both a scientific and technological perspective. Some of them have successfully led to applications in information storage industry. This thesis theoretically studies some of these structures and focuses on two aspects: (1) the effect of surface roughness in magnetoresistive devices, (2) spin transfer torque induced magnetization dynamics.

Surface roughness is known to be an important source of scattering in small structures. We employ Landauer's formalism to study spin dependent electron transport in structures like spin valve, magnetic tunnel junction and nanowires. An efficient algorithm is developed to solve the scattering problem numerically. It is found that the resistivity and magnetoresistance are strongly influenced by the surface roughness scattering.

The coupling between spin polarized current and local magnetic moment results in a torque on the magnetization. This induces dynamic effects such as magnetization reversal and switching. We propose an exchange coupled composite structure to study current induced reversal and show that this structure can significantly reduce the critical current.

The spin torque can cancel the damping torque and induce steady precession. This type of spin torque oscillator is attractive as a microwave device at the nanoscale. Several of these oscillators can couple together and oscillate in a phase coherent manner. The mechanism for the coupling is studied analytically and using micromagnetic simulation. It is found that the coupling exhibits an oscillatory behavior through a spin wave mediated interaction.

Contents

Abstract . . . ii

Contents . . . iv

List of figures . . . vi

1 Introduction **1**

1.1 Spin and ferromagnetism . . . 1

1.2 Spin dependent transport and giant magnetoresistive effect . . . 3

1.3 Surface roughness in magnetoresistive devices . . . 9

1.4 Spin transfer torque . . . 9

1.5 Modeling of spin transport and magnetodynamics . . . 12

1.6 Surface roughness scattering in nanostructures . . . 16

1.7 Current induced dynamics in magnetic nanostructures . . . 17

2 Spin transport in nanostructures **25**

2.1 Quantum transport theory . . . 25

2.2 Effect of pinholes in magnetic tunnel junctions . . . 29

2.3 Surface scattering in nanowires 36

2.4 Surface scattering in magnetic nanostructures 50

2.5 Conclusions 58

3 Exchange assisted spin torque switching 61

3.1 Introduction 61

3.2 Exchange assisted switching 63

3.3 Conclusions 71

4 Phase locking of spin torque oscillators 72

4.1 Introduction 72

4.2 Analytical theory 74

4.3 Micromagnetic simulation 77

4.4 Conclusions 86

References 88

List of Figures

1.1 Density of states of BCC Fe, calculated using Vienna ab-initio simulation package (VASP). 4

1.2 Geometry of CPP GMR sandwich structure. 7

1.3 Resistivity hysteresis loop of a Co/Au/Co loop [1]. 8

1.4 Spin transfer torque in a magnetic multilayer structure. 11

1.5 Schematic of damping and spin torque. 19

1.6 Field and current switching on the same metallic multilayer [2]. . . . 20

1.7 Experimental observed power spectrum in double point contact geometry, where the two peaks merged into a single one when synchronization happens [3]. 24

2.1 Schematic plot of a MTJ harboring a pinhole. 31

2.2 Consider a pinhole of one atom in diameter and 1nm (4 atom) long embedded in a MTJ. (a) shows the conductance (measured in $\frac{e^2}{h}$) vs. energy of incoming electron in the parallel alignment (PA) for both majority and minority spin bands; (b) is G vs. E for antiparallel alignment (APA); in (c) nonlinear I-V characteristic is plotted for both PA and APA configuration; (d) shows the MR dependence on bias voltage. 34

2.3 Same quantities are plotted as in Fig. 2.2 after averaging over an ensemble of pinholes. 37

2.4 The MR of a wide pinhole of 5 atoms in diameter compared with an all-metal GMR spin valve. 38

2.5 Sample calculation of normalized resistance $R/(\frac{\hbar}{e^2})$ as a function of length for a 3D wire of $2.5nm$ wide. MFP $l \approx 0.46nm$ is obtained in the linear regime. The onset of localization occurs around $L \approx Ml = 30nm$. 43

2.6 The MFP as a function of Fermi energy. 44

2.7 MFP as a function of wire width in the strong scattering regime ($\Delta > 1eV$) for two different surface fluctuations: $\sigma = 0.125nm$ in (a) and $\sigma = 0.25nm$ in (b). The solid and dashed lines are the linear fit to the data. 46

2.8 MFP vs. width in the weak scattering regime $\Delta = 0.5eV$ as compared to the analytical results in Eq. 2.8. 48

2.9 MFP's dependence on impurity potential Δ in a 12 atom by 12 atom wire. For weak scattering ($\Delta \lesssim 1eV$), $l \propto \frac{1}{\Delta^2}$ as expected from Eq. 2.8. As Δ increases, the MFP approaches a nonzero constant. 49

2.10 Magnetoresistance as a function of resistance-area product (by varying barrier thickness) for different surface roughness. 52

2.11 (a). Schematic view of a barrier with a notch. (b) and (c), MR ratio and RA product as function of notch depth. 54

2.12 (a). Resistance vs. wire length for parallel alignment (PA) and anti-parallel alignment (APA) for a nanowire-based GMR device with two different roughnesses. (b). Magnetoresistance as a function of wire length. 55

2.13 (a). Resistance vs. wire length for parallel and anti-parallel alignment for nanowire based GMR device. (b). Magnetoresistance as a function of wire length. 56

2.14 (a): Schematic plot of a fabricated notch in front of the barrier. (b) The resistance as a function of notch-barrier separation L. (c) Magnetoresistance vs L. 57

3.1 The exchange coupled composite structure proposed to reduce switching current. 64

3.2 The dynamic phase diagram of the double layer structure. 67

3.3 The composite structure consisting multiple soft assisting layers with graded anisotropy. 68

3.4 The switching current as a function of inter-layer exchange coupling, for different number of assisting layers. 69

3.5 The switching current as a function of damping constant in the assisting layers, for different number of assisting layers. 70

4.1 (a) Calculated dependence of peak frequency on wire width (circles) with a linear fit (solid line) and experimental results extracted from [4]. (b) a snap-shot of the steady state SW configuration generated by the point contact. 79

4.2 Phase-lock of two STOs spaced at 500 nm. The current of one contact is fixed at $I_1 = 4.5$mA, while I_2 is varied. (a) The map of PSD versus the frequency and I_2. (b) For $I_2 = 4.6$mA, the two contacts are phase-locked with a single peak and significantly larger output power. (c) For $I_2 = 4.2$mA, the two contacts are not phase-locked and two distinct peaks are shown. 81

4.3 The map of the combined power spectrum from both contacts versus frequency and distance R_{12}. The oscillation of output signal is caused by the oscillating coupling parameter $K(R_{12})$. The period is about 34nm that matches the estimated SW wavelength. 82

4.4 Calculated dependence of phase difference on frequency difference using Eq. 4.6 (line) and simulation (+) for $R_{12} = 100$nm (a) and $R_{12} = 188$nm (b). Snapshot of the respective SW configuration shown in (c) and (d). (e) shows the coupling parameter $K(R_{12})$ from simulation using and theoretically evaluated using $K(R_{12}) = \mathrm{Im}[(\frac{\gamma}{1-i\alpha}H_{ex} - \omega_1)cH_0^{(2)}(k_1R_{12}) + (\frac{\gamma}{1-i\alpha}H_{ex} - \omega_2)cH_0^{(2)}(k_2R_{12})]$. 84

4.5 Simultaneous variation of currents under both contacts while keeping $I_1 = I_2$. (a) The blue shift of peak frequency with increasing current. (b) The variation of the integrated power. 85

Chapter 1

Introduction

1.1 Spin and ferromagnetism

Spin is an internal degree of freedom of a particle that gives rise to its intrinsic angular momentum. Particles with spin possess a magnetic dipole moment, just like a circulating charge in classical electrodynamics. The magnetic moment μ of a particle with mass m, charge q, angular momentum J and g-factor g is:

$$\mu = \frac{gq}{2m} J, \tag{1.1}$$

For an electron in an atom, both the orbital motion and spin contribute to its angular momentum: $\vec{J} = \vec{S} + \vec{L}$. The spin is a quantum property in that the spin angular momentum is quantized. The quantization of spin was first observed in the Stern-Gerlach experiment, where a particle passing through a Stern-Gerlach appara-

tus is either up or down according to its spin. Spin operators obey a commutation relation that is similar to its orbital counterpart:

$$[S_i, S_j] = i\hbar\varepsilon_{ijk}S_k, \tag{1.2}$$

where ε_{ijk} is the Levi-Civita symbol.

The spin of a particle is crucial for its properties in statistical mechanics. Particles with half-integer spin, known as *fermions*, obey the Fermi-Dirac statistics, which forbids them to occupy the same quantum state, a restriction known as the Pauli exclusion principle. The average number of particle in a single state is:

$$n_i = \frac{1}{e^{(\varepsilon_i - \mu)/k_B T} + 1}, \tag{1.3}$$

Particles with integer spin, or *bosons*, on the other hand, obey Bose-Einstein statistics and the expected number of bosons occupying a single state is:

$$n_i = \frac{1}{e^{(\varepsilon_i - \mu)/k_B T} - 1}, \tag{1.4}$$

Ferromagnetism refers to a correlated state in which the electronic spins spontaneously align and exhibit long range order at the atomic level. Below a certain temperature known as the Curie temperature T_C, a ferromagnet becomes spin polarized and acquires a finite magnetization even in the absence of an external field. The microscopic mechanism for ferromagnetism is the quantum mechanical exchange interaction [5]. Due to the Pauli exclusion principle, electrons with parallel spins are

forbidden to occupy the same orbital state. This reduces the overlap of the electronic wavefunction with parallel spins. Therefore the electric charges on neighboring atoms are further apart in space, which decreases the electrostatic energy between electrons. This interaction is several orders of magnitude stronger than the magnetostatic dipole-dipole interaction between neighboring atoms. In ferromagnetic materials, the density of states of spin-up and spin-down band is shifted with respect to each other as a result of the exchange splitting Fig.1.1.

As mentioned earlier, the magnetic moment may come from two sources: the intrinsic angular momentums of electrons, i.e. spin, and the orbital moment. In transitio metals, the orbital moment is quenched due to crystal field splitting [5]. Therefore the magnetization in a ferromagnet is dominated by the spin contribution. Ferromagnetic materials often exhibits anisotropic behavior [6], i.e. the magnetization prefers to align in certain direction. The crystalline anisotropy caused by the spin-orbit interaction or the shape anisotropy caused by magnetic dipole interactions pin the equilibrium magnetization in a certain axis or plane.

1.2 Spin dependent transport and giant magnetoresistive effect

The extensive study of spin dependent transport began in 1988 when the giant magnetoresistive effect (GMR) [7, 8] was discovered. The discovery marks the beginning

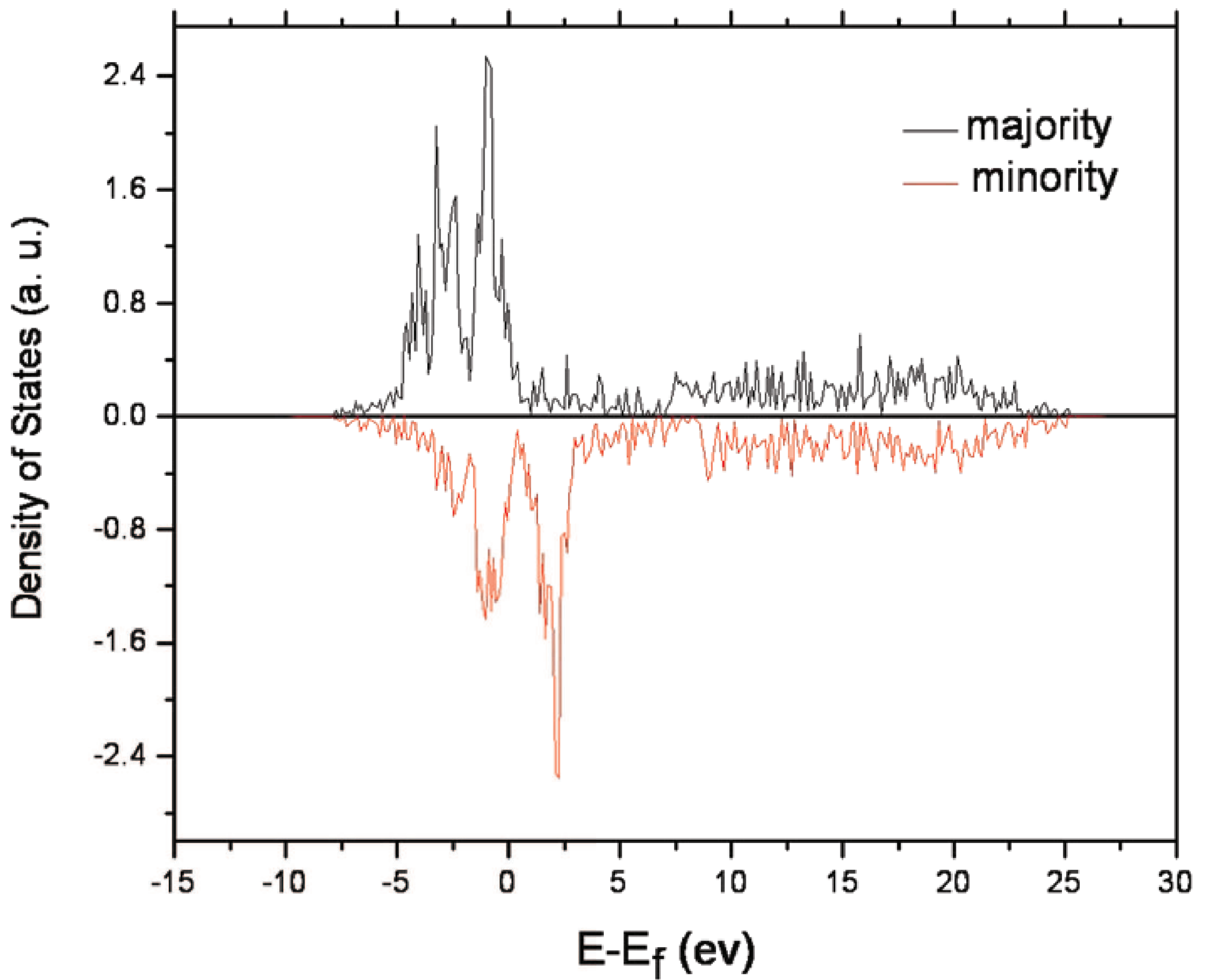

Figure 1.1: Density of states of BCC Fe, calculated using Vienna ab-initio simulation package (VASP).

of effort to utilize the spin degree of freedom in electronics. The GMR effect occurs in a structure consisting of multiple magnetic layers, and the resistance changes when the relative orientation of magnetization in these layers changes. For example, let us consider a sandwich structure including two magnetic layers separated by a metallic layer as in Fig. 1.2. When the magnetizations in two magnetic layers are anti-parallel, the resistance is relatively high. The sample has a lower resistance when the magnetizations are parallel. The thickness of the metallic spacer can be adjusted to make the magnetic layers anti-ferromagnetically coupled and, consequently, the magnetization anti-parallel. An external field can be applied to bring the magnetization into parallel alignment. In this way, the resistance shows a hysteresis behavior in an external field, as shown in Fig. 1.3 for a Co/Au/Co structure [1].

What lies at the heart of GMR effect is the spin filtering effect. A spin filter, similar to an optical polarizer, can convert a beam of electron with undefined spin polarization into one with well-defined polarization. Any ferromagnetic metal can serve as a spin filter for an electric current. When a beam of electrons pass through a ferromagnetic material, the conducting electrons can no longer be distinguished from electrons originally possessed by the ferromagnet and they acquire a spin polarization according to the exchange split density of states e.g. Fig.1.1. To explain the GMR effect, and for the sake of clarity of argument, let us consider a perfect spin filter that acts as a conductor for electrons of one spin orientation, but as an insulator to those of the opposite orientation. Such materials, known as half-metals, exist in reality and

are capable of producing 100% spin polarized current. Now first consider a magnetic sandwich structure with parallel magnetizations (Fig.1.2), assuming perfect filtering; electrons with spin pointing to the right can pass through both layers, while spins pointing to the left are blocked. When the magnetizations are anti-parallel as shown in Fig.1.2 on right, the bottom layer only allows electrons with spin pointing to the left to go through, and it reflects all the electrons with spin pointing to the right. After electrons pass the first layer, the current is 100% polarized with spin pointing to the left. However, the top layer can only conduct electrons with spin pointing to the right. Therefore no electron can go through both layers, and the whole structure has a high resistance compared to that of the parallel alignment. The states in between parallel and anti-parallel alignment have intermediate resistance, as expected.

In the GMR structure, the spacer separating magnetic layers is a thin metallic layer such as Cu. What if we replace the metal spacer with an insulating barrier? It turns out this arrangement can produce an even more significant magnetoresistance (MR). The enhancement of MR compared to the GMR case mainly results from a spin dependent tunneling effect. In a ferromagnet, the electron bands are split and, therefore, the wavelength of spin up electrons at the Fermi level is different from that of spin down electrons. On the other hand, from quantum mechanics, the transmission probability of a particle tunneling through a barrier is given by:

$$T = Ce^{-2\kappa L}, \tag{1.5}$$

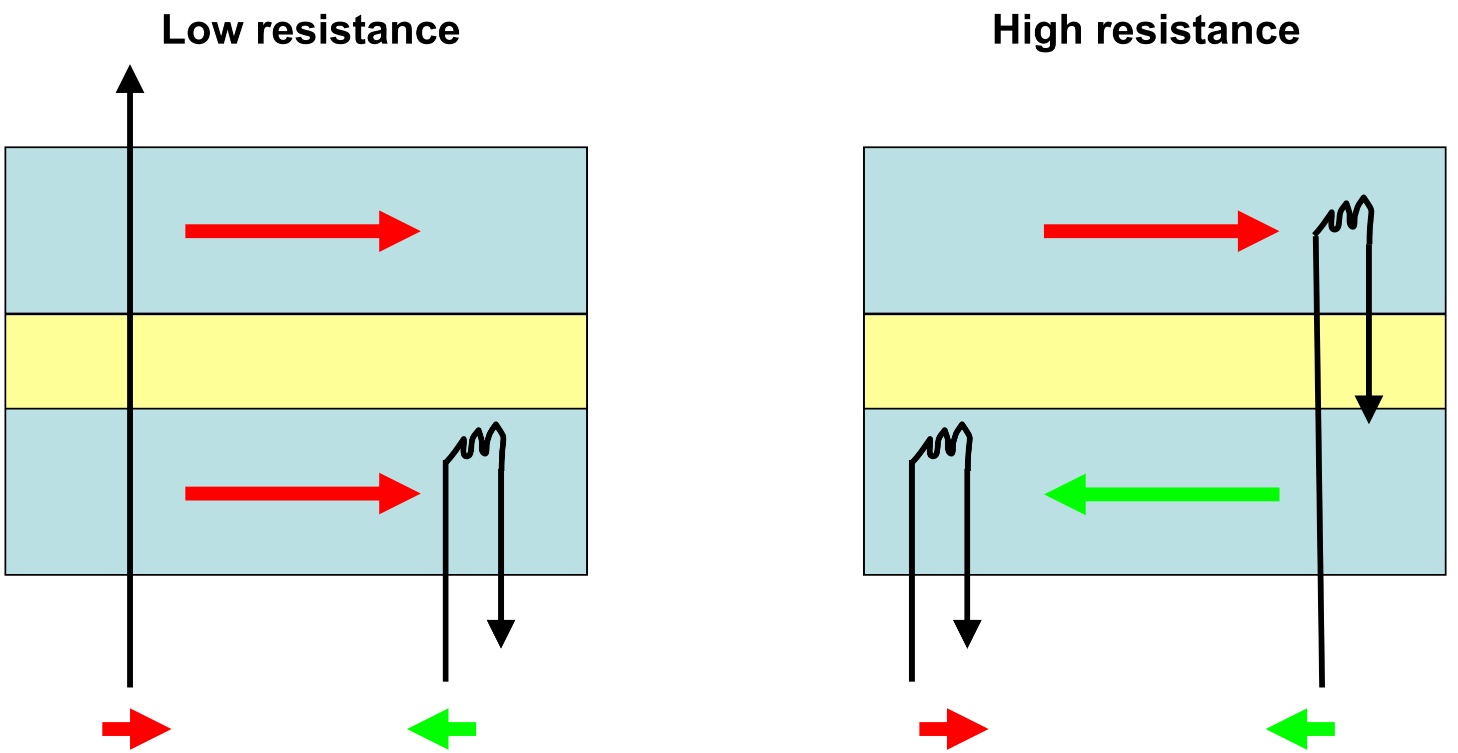

Figure 1.2: Geometry of CPP GMR sandwich structure.

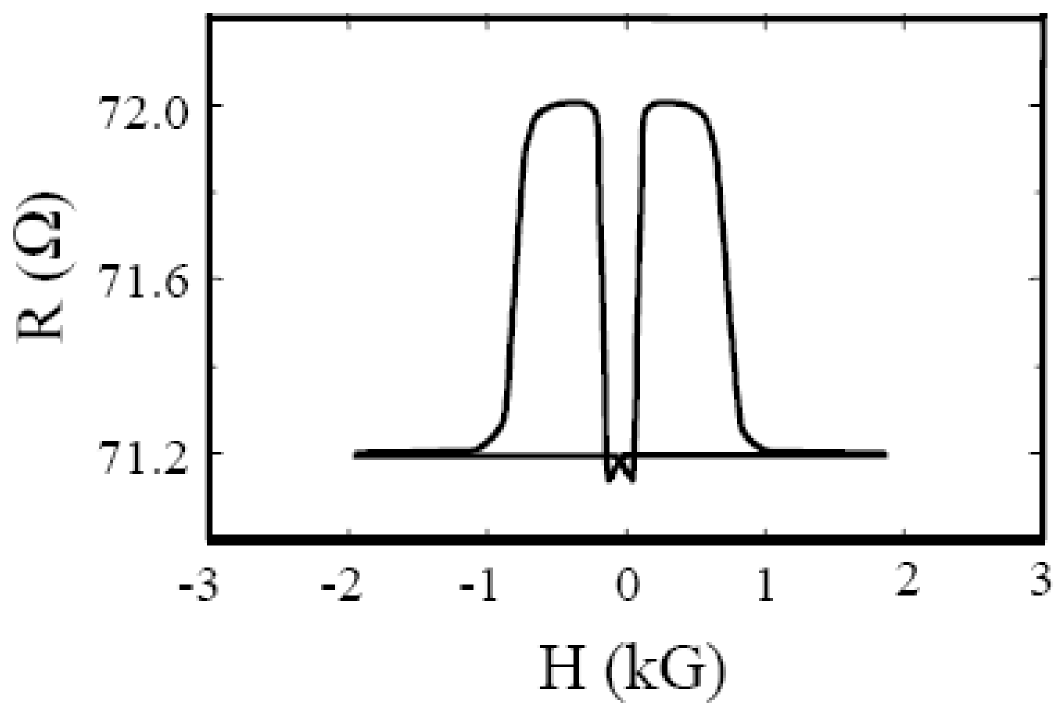

Figure 1.3: Resistivity hysteresis loop of a Co/Au/Co loop [1].

κ is the wave vector of the particle and L is the barrier thickness. From the above equation, it is clear that tunneling probability depends on the particle's wavelength and consequently its spin. A substantial tunnel magnetoresistance (TMR) at room temperature was first observed in 1995 in magnetic tunnel junctions (MTJ) [9, 10], where magnetic layers are separated by a tunnel barrier. In the early studies of MTJs, disordered aluminum oxide was used as the tunnel barrier. Butler *et al.* [11] calculated the tunneling property of Fe/MgO/Fe structure and found that the symmetry of the relevant electronic states can lead to a extremely high TMR. Following the prediction, the TMR has continued to increase rapidly in MgO-based MTJ until today. The high sensitivity of resistance to magnetic field in GMR and MTJ structures makes them extremely valuable field sensing devices. Indeed, soon after the initial discovery, these devices were widely used as field sensors in magnetic hard drives to detect the small field from the disk surface. They have played an essential role in boosting the storage density.

1.3 Surface roughness in magnetoresistive devices

1.4 Spin transfer torque

As discussed above, magnetic materials tend to selectively pass electrons based on its spin. Therefore, the magnetization plays a role in the transport of conducting electron. The flip side of the spin filtering effect is that the conducting electron has

an influence on the magnetization of the magnet. To see this, let us again consider a magnetic sandwich structure consisting of perfect spin filters. After the electron passes through layer FM_1, as shown in Fig. 1.4, its spin is polarization becomes parallel to M_1 and can be decomposed into components that are parallel and perpendicular to M_2. Since FM_2 is a perfect spin filter, the polarization of electrons emerging after passing FM_2 must be parallel to M_2. Comparing the spin polarization of electron before and after entering FM_2, we find that the perpendicular component $s_\perp$ appears to vanish. In fact $s_\perp$ does not simply disappear, instead it is transferred into FM_2. The conservation of angular momentum requires that the magnetization recoils as it rotates the spin of the conducting electron. Essentially, the transfer of angular momentum from conducting electron to magnetization results in a torque proportional to $\sin\theta$ and this torque is named spin transfer torque (STT). By reversing the sign of the current, we can generate a torque in the opposite direction, in which case it is the *reflected* electrons from FM_1 that carry the spin information.

In 1996, Berger [12] and Slonczewski [13] independently predicted that current flowing perpendicular to the plane in a magnetic multilayer can excite spin waves and generate a torque that is strong enough to reorient the magnetization. The predictions marked the beginning of the study of STT and have stimulated much theoretical and experimental work in the past decade. With a large enough current, the spin torque can overcome the damping torque and switch the magnetization [14, 15]. In current induced switching experiments, one magnetic layer serves as the reference layer that

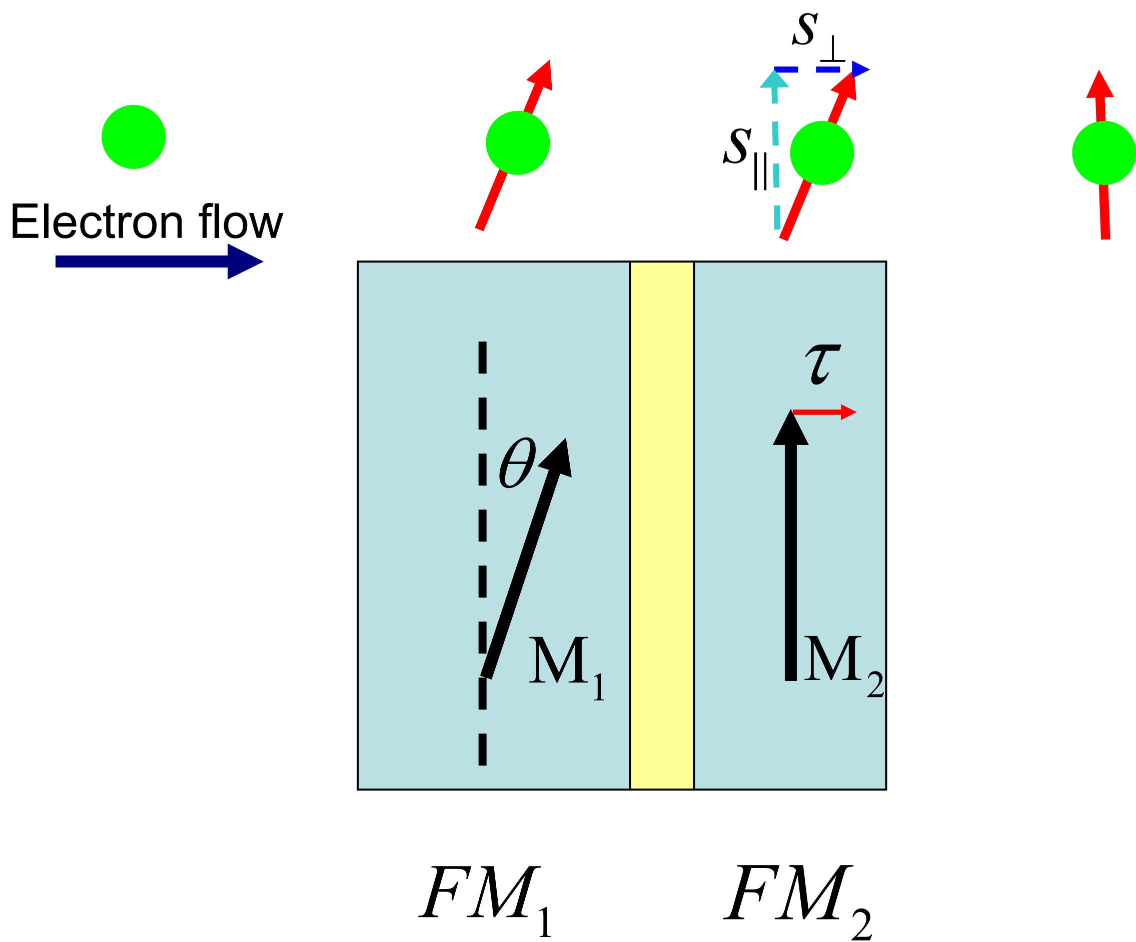

Figure 1.4: Spin transfer torque in a magnetic multilayer structure.

polarizes the current, the other layer is the free layer to be switched. The reference layer is required to have a larger coercivity than the free layer, which can be achieved by having its magnetization pinned through exchange bias or simply having a larger thickness. By applying an intermediate current, one can make the spin torque exactly balance the damping torque, in which case the magnetization will undergo a steady precession [16]. The STT effect not only occurs in multilayers, but also in a structure where magnetization changes continuously. For example, it has been demonstrated that current can be used to drive the domain wall in a magnetic nanowire [17].

1.5 Modeling of spin transport and magnetodynamics

The modeling of ferromagnetism is often concerned with two classes of problems. First, we are interested in how the charge and spin of an electron are transported in a ferromagnetic metal. Second, we are interested in the equilibrium configuration of magnetization and its dynamic response to the presence of a external field or spin polarized current.

To study the first class of problems, the electronic property in transition metals can be accurately described using the local spin density approximation (LSDA) based on density functional theory. Using such a first principle calculation, many properties such as the magnetic moment can be accurately calculated without any fitting

parameters. Simplified models have been developed to capture the essential physics of ferromagnetism. One particularly useful model of this type is the s-d model, where "s" electrons represent the delocalized band state that is responsible for transport and "d" electrons describes the localized magnetic state. The s electron is assumed to have a free electron band and coupled to the d electron through a weak local interaction:

$$H_{s-d} = -J_{ex}\vec{s} \cdot \vec{S} \tag{1.6}$$

$\vec{s}$ is the spin polarization of the itinerant electron, $\vec{S}$ is the magnetic moment of the localized electron and J_{ex} represents the exchange coupling. In transition metals there is strong hybridization between s bands and d bands, and the d electron can not be regarded as localized. So the s-d model is far from being realistic. However, simplified models can be very useful to illustrate physical concepts.

To study the equilibrium and dynamic properties of magnetization, the most frequently adopted method is *micromagnetics*, which treats the magnetic moment as a classical variable instead of as many quantum mechanical spins. This can be justified by noticing that the exchange coupling between atomic spins is so strong that most interesting dynamics happens on a length scale that is much longer than the atomic spacing. Essentially, many spins are tightly bonded together to form a *macrospin* whose spin quantum number is large enough to be considered as classical. Because of the strong exchange coupling the magnetization $\vec{M}$ is treated as having a fixed length. The total effective field experienced by the magnetic moment is obtained

by taking the functional derivative of the free energy with respect to the magnetization: $\vec{H}_{eff} = -\delta E/\delta \vec{M}$. Typically, the free energy contains the interaction with the external field, crystalline anisotropy, dipole-dipole interaction and the Heisenberg exchange interaction, which can be written explicitly as:

$$\begin{aligned} E = -\int d^3r \vec{H}_{app} \cdot \vec{M}(\vec{r}) - \frac{K_u}{M_S^2} \int d^3r (\hat{n} \cdot \vec{M}(\vec{r}))^2 + \frac{A_{ex}}{M_S^2} \int d^3r \left| \nabla \vec{M}(\vec{r}) \right|^2 \\ -\frac{1}{8\pi} \int d^3r \int d^3r' \vec{M}(\vec{r}) \cdot \frac{3(\vec{M}(\vec{r}') \cdot \vec{x})\vec{x} - \vec{M}(\vec{r}') \left|\vec{x}\right|^2}{\left|\vec{x}\right|^5}, \end{aligned} \tag{1.7}$$

where $\vec{x} = \vec{r} - \vec{r}'$, M_S is the saturation magnetization, A_{ex} is the exchange constant, $\hat{n}$ is the easy axis direction of the uniaxial anisotropy and K_u is the anisotropy constant.

The equation of motion for magnetization satisfies the torque equation:

$$\frac{\partial \vec{M}}{\partial t} = \vec{T}_{tot}, \tag{1.8}$$

where $\vec{T}_{tot}$ is the total torque acting on the magnetization. One contribution to $\vec{T}_{tot}$ is the torque $\vec{T}_{eff} = -\gamma \vec{M} \times \vec{H}_{eff}$ produced by the effective field, where γ is the gyromagnetic ratio. It makes the magnetization precess around $\vec{H}_{eff}$. In reality, such precession is not sustainable without a supply of external energy. The magnetic energy will dissipate through the coupling between spin and other degrees of freedom in the system. To describe such dissipation process, an additional damping torque needs to be included in the dynamic equation. Such damping torque usually comes with two varieties: the Landau-Lifshitz damping $\vec{T}_{LL} = -\frac{\alpha\gamma}{M_S} \vec{M} \times (\vec{M} \times \vec{H}_{eff})$ and the Gilbert damping $\vec{T}_G = \frac{\alpha}{M_S} \vec{M} \times \frac{\partial \vec{M}}{\partial t}$, where α is the dimensionless damping con-

stant. The effect of both is to relax the magnetization until local energy minima are reached. Furthermore, it can be shown that T_{LL} and T_G are equivalent to each other by renormalizing the gyromagnetic ratio by a factor of $1/(1+\alpha^2)$. Notice that both $\vec{T}_{eff}$ and the damping torque conserve the magnitude of the macrospin. However, $\vec{T}_{eff}$ preserves the magnetic energy while the damping torque always reduces it.

In the presence of a spin polarized current, the exchange interaction between the spin polarization of current and the magnetization produces an additional spin torque. Within the s-d model [18], the spin torque can be written as:

$$T_{ST} = -\frac{b_J}{M_S^2}\vec{M} \times (\vec{M} \times \frac{\partial \vec{M}}{\partial x}) - \frac{c_J}{M_S}\vec{M} \times \frac{\partial \vec{M}}{\partial x}, \tag{1.9}$$

where magnetization is assumed to vary in the x direction, and b_J and c_J characterize the strength of the spin torque. The first term in 1.9 corresponds to the process in which the spin of the conducting electron *adiabatically* follows the local magnetization and is called the *adiabatic torque*. The second term in 1.9, represents a correction to the adiabatic process which takes into account the fact that the conducting electron spin mistracks the magnetization.

1.6 Surface roughness scattering in nanostructures

In conventional electronics, the device size is usually large compared to the mean free path (MFP) and it is therefore sufficient to understand the transport behavior based on the bulk properties of the material. With the constant need for smaller products and the progress of nano-fabrication, devices today are routinely made at nano-scale and reach a size comparable to the MFP. Also the development of thin film technology makes it possible to fabricate devices based on various multilayer and nanopillar structures. In these small devices, the surfaces and interfaces between layers are expected to play an increasingly important role, which requires us to understand how surfaces influence electron transport. In most of the experimental techniques, surface roughness is inevitable. Consequently, the main influence of the surface on electron transport is rough surface scattering (RSS). First of all, RSS changes the metallic properties of the device, such as the MFP and resistivity. There have been intense study of the role of RSS in metallic nanowire and silicon nanowire transistors [19]. In magnetoresistive devices such as MTJ, the interface roughness significantly modifies the magnitude of MR and its voltage dependence. For example, in an MgO based MTJ, first principle calculations predicts an MR of order 10000% [11]. There has been much progress in making an MTJ with high TMR and the highest TMR reported to date is 1056% at room temperature [20]. Despite these great achievements, the

obtained TMR is still much below the theoretical limit. This discrepancy may be due to the RSS: interface scattering breaks the symmetry of the surface state and reduces the TMR [21]. The rough surface scatters the transport electrons and influences both the metallic and magnetic properties of the device.

1.7 Current induced dynamics in magnetic nanostructures

Magnetism has a long history of being utilized by mankind to push forward technology and civilization, from the compass used by ancient Chinese for navigation to the modern day hard drive for information storage. Essentially, these applications all involve the manipulation of magnetic moment in the material by a magnetic field. STT provides a new way to manipulate magnetization using electric current rather than field. STT gives rise to many magnetodynamical phenomena that have never been investigated before, including current induced switching, spin torque oscillation and current driven domain wall motion, to name a few, which are not only fundamentally interesting, but also attractive for future applications. The understanding of these novel effects poses a tremendous challenge for condensed matter physics, which requires a deeper understanding of the spin transport process. Although we are still far away from the full comprehension, a coherent physical picture is emerging [22]. On the other hand, questions naturally arise as to the possibility of utilizing these

new effects to make useful devices. In this section, I am going to give a brief overview of the experiments and possible applications for some of the STT induced effects.

According to the theory of STT [18], the spin torque can be either parallel or anti-parallel to the damping torque, depending on the direction of spin polarization. When STT is in the opposite direction of damping torque Fig. 1.5, it may cause instability, as predicted by Slonczewski [13]. If the current is sufficiently strong, the STT can permanently reorient the magnetization in a new state [14, 15]. The main probe to detect the STT induced magnetization dynamics is resistance measurement, which reflects the magnetic alignment through the GMR effect. The similarity between field and current induced switching in a GMR multilayer is demonstrated by Braganca et. al. [2], as shown in Fig. 1.6. Despite such similarity, it is important to note that the mechanism of field switching is different from STT switching. In the former case, the application of field changes the energy landscape of the system and the magnetization relaxes to the lowest energy state through damping. In the STT case, however, the torque is non-conservative, namely it does not result from the magnetic energy of the system itself. Instead, STT happens because the angular momentum is pumped into the system from a external source i.e. the conducting electrons.

The current induced switching effect has been proposed as a writing technique in magnetic random access memory (MRAM). A MRAM consists of an array of MTJs and each MTJ stores one bit of information through magnetic alignment. The anisotropy makes MRAM non-volatile, namely no energy is required to retain infor-

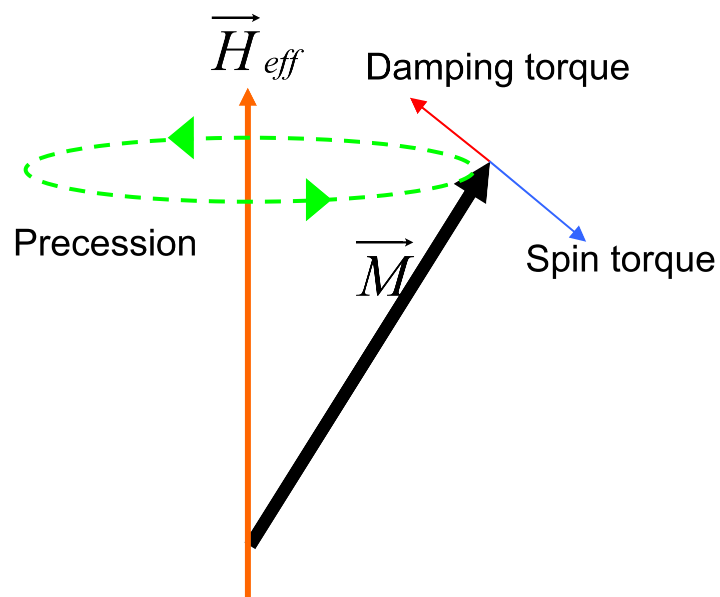

Figure 1.5: Schematic of damping and spin torque.

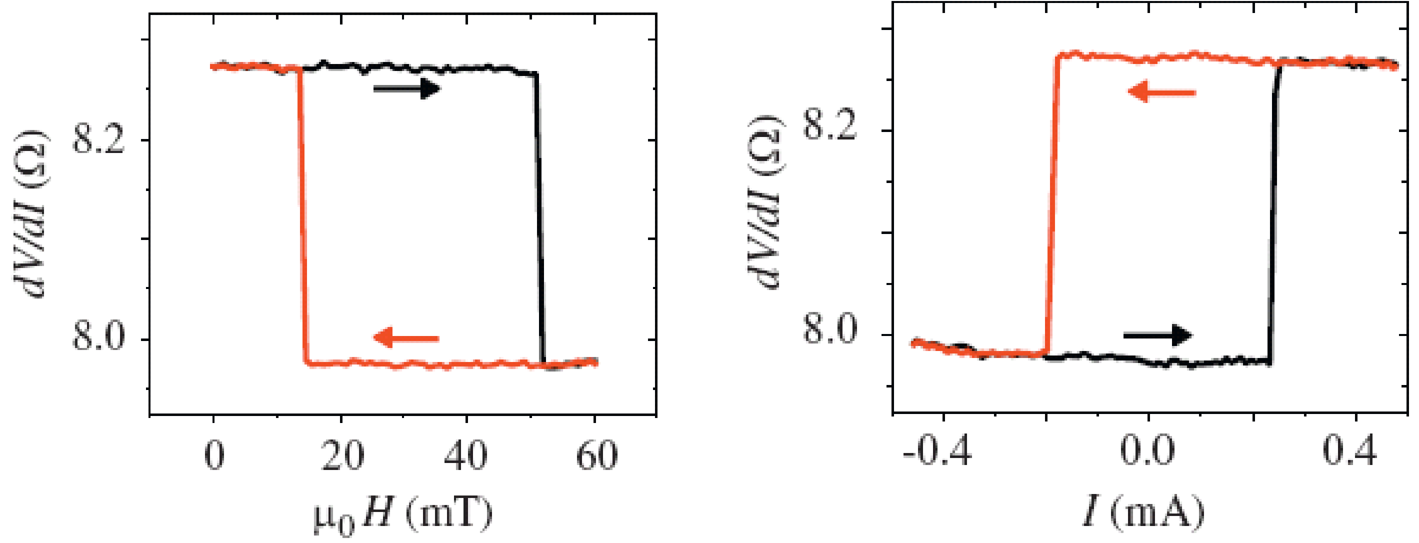

Figure 1.6: Field and current switching on the same metallic multilayer [2].

mation, which is a big advantage of MRAM technology. For readback, the tunneling magnetoresistance of an MTJ is used. In an earlier version of MRAM, writing was achieved by applying a current which in turn generates a magnetic field that switches a bit state. However, this method has a problem when scaling to small dimensions. As the bit size shrinks, the writing field is expected to influence neighboring bits. A promising alternative is to directly inject current into the MTJ and switch the bit using STT. The advantage of STT is that each bit can be locally controlled and therefore has the potential for high density storage. In order to achieve the highest recording density, it is required that the switching current be provided by a transistor that has a channel width equal to the MTJ size. Assuming the transistor can carry 0.5mA of current per channel width, a switching current density of $5 \times 10^5 A/cm^2$ is needed. In the conventional MTJ, magnetization lies in-plane due to the demagnetization field. The switching current is:

$$J_C = \frac{2e\alpha}{\hbar\eta} M_S t(H_{appl} + H_K + 2\pi M_S), \tag{1.10}$$

where η is the spin torque efficiency, α is the damping parameter, H_{appl} is the applied field along easy axis, H_K is the in-plane uniaxial anisotropy field. For soft material such as permalloy, the demagnetization field $2\pi M_S$ is the dominating term. The switching current for in-plane MTJ is over $10^7 A/cm^2$ [23]. On the other hand, this term does not contribute to the thermal stability of the memory cell. Therefore, it is natural to use a perpendicular anisotropy $H_{K\perp}$ to balance $2\pi M_S$ and align the

magnetization out of plane. In this geometry, the switching current density becomes:

$$J_C = \frac{2e\alpha}{\hbar\eta} M_S t (H_{K\perp} - 2\pi M_S). \tag{1.11}$$

To reach the goal of $J_C \simeq 5 \times 10^5 A/cm^2$, while maintaining the thermal stability, a breakthrough is still required. In this thesis, I will propose and study a method to lower J_C using an exchange composite structure.

Another promising direction for applying STT is current induced precession. The magnetic moment tends to precess around the effective field, an effect known as the Larmor precession. Generally, in order to have a steady precession, one has to supply energy into the moment to balance the energy dissipation through damping. Conventionally, this is realized by applying a time varying field such as in ferromagnetic resonance. As discussed earlier, the STT can be anti-parallel to the damping torque and potentially provides a new route for generating precession, as observed in a metallic multilayer [16]. Resistance measurement is again used to probe the dynamics through the GMR effect, where the precessing magnetization generates a oscillating voltage. Essentially, this device, the spin torque oscillator (STO), converts a DC current into an AC signal. The STO offers the possibility of making a nano-scale microwave source with frequency tunability, which has potential application for wireless on-chip and chip-to-chip communication.

The initial experiment of STO was done in nanopillars in the presence of a large magnetic field [16]. Before it can be useful in practice, it is crucial to eliminate the

external field. Currently, this is still an open problem under intensive investigations. There has been demonstration of STO using high perpendicular anisotropy material as a polarizing layer without any applied field [24]. Another technical challenge for applications to overcome is increasing the output power. To increase the power of an individual STO, one can use materials with higher polarization and MR, such as MTJ based STO. Another path to boost the power level is through the synchronization of multiple oscillators: if N STOs are phase locked the power increases quickly as N^2. This is exactly how a group of fireflies make themselves highly visible at night: although an individual firefly can only generate a very weak blink, many of them, through some coordination mechanism, are able to emit light flashes in perfect synchronicity. In a point contact geometry, phase locking and synchronization have been demonstrated for two oscillators [25, 3]. By fixing the precession frequency of one oscillator and continuously changing the other one, Kaka and collaborators observed that when the two frequencies are sufficiently close, the two peaks in the spectrum merged into a single one with a much narrower width, see Fig. 1.7. In a subsequent experiment, the NIST group showed that the spinwaves propagating in the continuous free layer are responsible for the phase locking. There are other ways to realize phase locking and synchronization for STOs, such as through electrical contact [26] and coupling to a external source [27].

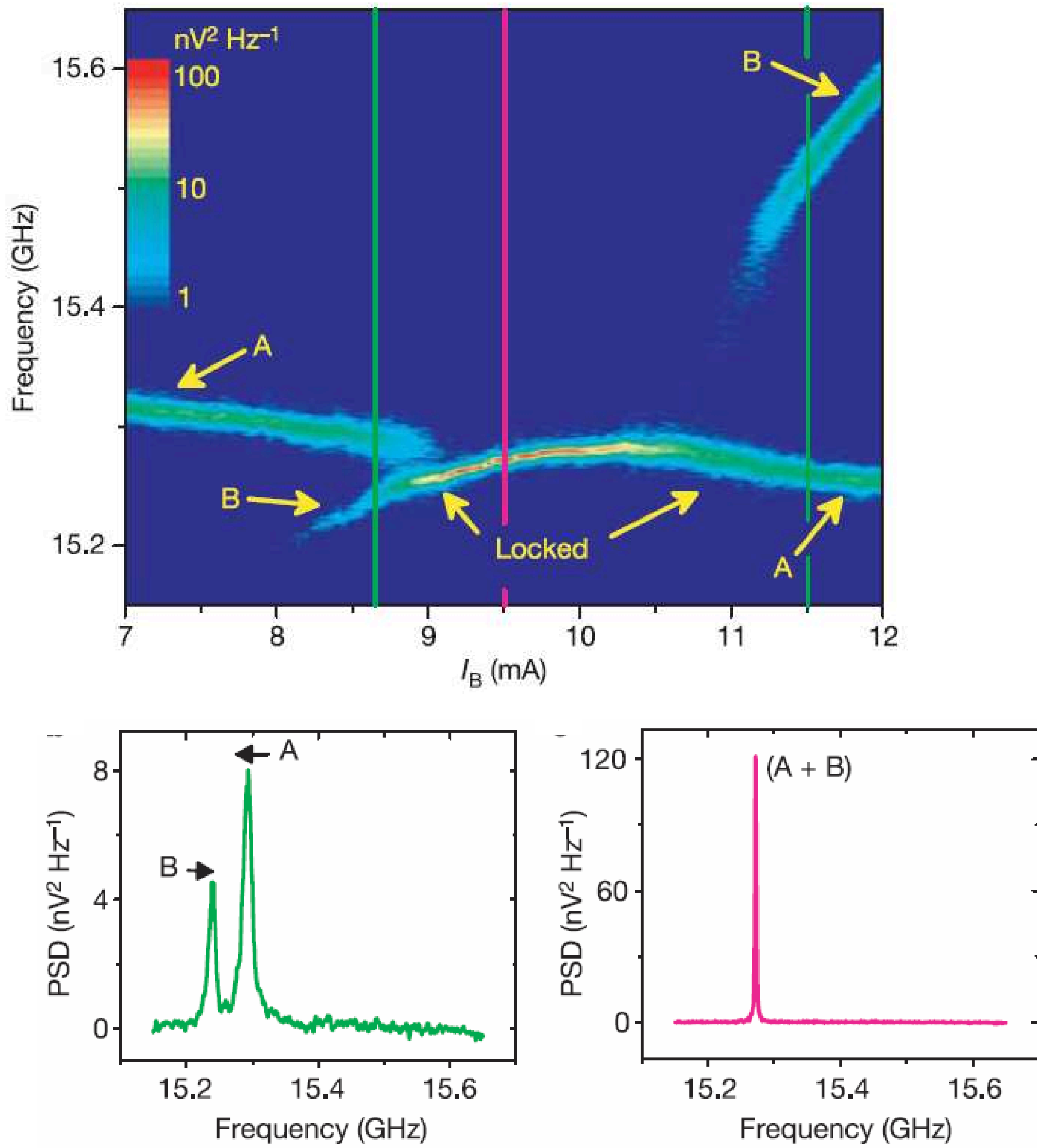

Figure 1.7: Experimental observed power spectrum in double point contact geometry, where the two peaks merged into a single one when synchronization happens [3].

Chapter 2

Spin transport in nanostructures

2.1 Quantum transport theory

Classically, the conductance of a piece of conductor follows the Ohm's law:

$$G = \sigma \frac{W}{L},$$

where G is the conductance, σ is the conductivity, W is the width, and L is the length of the conductor. With the advance of fabrication techniques, it becomes possible to make a small conductor and explore the electron transport at a microscopic level. When the dimension of the conductor approaches a certain characteristic length scale, such as the mean free path, quantum mechanical effects become evident and Ohm's law may no longer be valid. In a point contact, for example, the conductance is quantized and each step is associated with the opening of an additional conducting channel (1D sub-band). In order to explain the transport phenomena associated

with nano-scale structures, a new theoretical framework that takes into account the quantum mechanical nature of the transport process is needed. An extremely fruitful and intuitive appealing approach was developed by Landauer [28], where the current flow is viewed as a transmission process. In the simplest case, the sample of interest is connected on both sides to one-dimensional leads, which serve as electron reservoirs. The conductance is given by the Landauer's formula:

$$G = \frac{2e^2}{h}T.$$

Here $\frac{e^2}{h}$ is the fundamental quantum of conductance, the factor of 2 accounts for spin degeneracy, and T is the transmission probability of the sample. The Landauer formula can be generalized to incorporate multiple channels:

$$G = \frac{2e^2}{h}\sum_{k_\parallel,k'_\parallel} t_{k_\parallel,k'_\parallel} t^*_{k'_\parallel,k_\parallel},$$

where $t_{k_\parallel,k'_\parallel}$ is the transmission amplitude of an incoming electron in transverse mode $k_\parallel$ exiting in transverse mode $k'_\parallel$.

The transmission amplitude can be calculated using the Green's function $t_{k_\parallel,k'_\parallel} = i\sqrt{v_{k_\parallel} v_{k'_\parallel}}\mathcal{G}^R(L,k_\parallel;R,k'_\parallel)$ [29], where $\mathcal{G}^R = \frac{1}{E-H+i0^+}$ is the retarded Green's function and $v_{k_\parallel}$ is the velocity of electron at the Fermi level in transverse mode $k_\parallel$.

In order to get the Green's function, we need to carry out matrix inversion, which is the most computationally intensive part. The structure being considered consists of $M\times M\times N$ atoms, with M being the width and N being the length. Straightforwardly, we can directly invert the matrix of dimension $M^2N \times M^2N$. The Green's function

generated this way contains mostly nonessential information because we only care about the matrix elements connecting the two ends of the structure. Alternatively, instead of dealing with the system as a whole, we can add in one layer at a time and calculate the Green's function recursively. This way, we can avoid calculating matrix elements not directly related to transmission coefficients and only need to invert a $M^2 \times M^2$ matrix one layer at a time for N layers. This leads to tremendous reduction of computational complexity, which we estimate in the following. The computational complexity to invert a $n \times n$ matrix using Gaussian elimination is $O(n^3)$, therefore, direct inversion has complexity of $O(M^6 N^3)$, compared to $O(M^6 N)$ using the recursive method. The recursive algorithm is especially efficient for systems with extended length, i.e. large N.

To illustrate this method, we consider the following example, in which the $n+1$ layer is connected to a piece containing n layers. The nearest coupling term between layer n and layer $n+1$ is represented by V.

We start with Dyson's equation:

$$\mathcal{G}^R = \mathcal{G}^{R0} + \mathcal{G}^{R0} V \mathcal{G}^R. \tag{2.1}$$

Here $\mathcal{G}^{R0}$ is the Green's function without coupling V and $\mathcal{G}^R$ is the total Green's function. The matrix element $\mathcal{G}^R_{m,n}$ is defined as $\mathcal{G}^R_{m,n} = \langle m| \mathcal{G}^R |n\rangle$ where $|n\rangle$ is the

wavefunction at layer n. Explicitly, each term in Eq. 2.1 takes the matrix form:

$$\mathcal{G}^{R0} = \begin{pmatrix} \mathcal{G}^{R0}_{1,1} & \cdots & \mathcal{G}^{R0}_{1,n} & 0 \\ \vdots & \ddots & \vdots & 0 \\ \mathcal{G}^{R0}_{n,1} & \cdots & \mathcal{G}^{R0}_{n,n} & 0 \\ 0 & 0 & 0 & \mathcal{G}^{R0}_{n+1,n+1}; \end{pmatrix}$$

$$\mathcal{G}^{R} = \begin{pmatrix} \mathcal{G}^{R}_{1,1} & \cdots & \cdots & \mathcal{G}^{R}_{1,n+1} \\ \vdots & \ddots & \vdots & \vdots \\ \vdots & \cdots & \mathcal{G}^{R}_{n,n} & \vdots \\ \mathcal{G}^{R}_{n+1,1} & \cdots & \cdots & \mathcal{G}^{R}_{n+1,n+1}; \end{pmatrix}$$

$$V = \begin{pmatrix} 0 & \cdots & \cdots & 0 \\ \vdots & \ddots & \vdots & 0 \\ \vdots & \cdots & 0 & V_{n+1,n} \\ 0 & 0 & V_{n,n+1} & 0. \end{pmatrix}$$

Expanding Dyson's equation 2.1 in terms of matrix elements, we obtain the following set of closed equations:

$$\begin{aligned} \mathcal{G}^{R}_{1,n+1} &= \mathcal{G}^{R0}_{1,n} V_{n,n+1} \mathcal{G}^{R}_{n+1,n+1} \\ \mathcal{G}^{R}_{n+1,n+1} &= \mathcal{G}^{R0}_{n+1,n+1} + \mathcal{G}^{R0}_{n+1,n+1} V_{n+1,n} \mathcal{G}^{R}_{n,n+1} \\ \mathcal{G}^{R}_{n,n+1} &= \mathcal{G}^{R0}_{n,n} V_{n,n+1} \mathcal{G}^{R}_{n+1,n+1} \end{aligned} \tag{2.2}$$

In Eq. 2.2, each term represents a $M^2 \times M^2$ matrix. After straightforward manipulation, we arrive at the recursive equation:

$$\mathcal{G}^{R}_{1,n+1} = \mathcal{G}^{R0}_{1,n} V_{n,n+1} \frac{1}{1-\mathcal{G}^{R0}_{n+1,n+1} V_{n+1,n} \mathcal{G}^{R0}_{n,n} V_{n,n+1}} \mathcal{G}^{R0}_{n+1,n+1} \tag{2.3}$$

Therefore, starting from just one layer and applying the above equation recursively, we can obtain the relevant Green's function $\mathcal{G}^{R}_{1,N}$ which connects both ends of the system and yields the conductance through Landauer's formula.

2.2 Effect of pinholes in magnetic tunnel junctions

With the techniques introduced in the previous section, we will apply them to the magnetic tunnel junction (MTJ) and, in particular, study the effect of pinholes. Magnetic tunnel junctions (MTJs) have drawn much attention during the last decade due to the large tunneling magnetoresistance effect (TMR) at room temperature [9, 10], which makes them attractive as magnetic field sensors and nonvolatile memory devices. A MTJ consist of an insulating layer sandwiched by two ferromagnetic (FM) electrodes and the electron tunneling rate depends on the relative magnetization alignment between FM layers. MTJs are replacing spin-valves as the read head in high density magnetic recording. The use of MTJ sense heads requires low resistance-area (RA) products and a reasonably high TMR, which is often obtained using an ultra-thin tunneling barrier, e.g. 1 nm. A longstanding issue in the fabrication of ultra-thin tunneling barriers is the formation of pinholes, where local barrier thickness is zero and the two FM electrodes make direct contact. A dominantly large percentage of current flows through metallic pinhole shorts rather than tunneling through the bar-

rier [30], so pinholes should change the properties of the MTJ substantially. It has been observed that MR decreases as the barrier thickness is reduced, suggesting surface roughness is responsible for the reduction of MR dimopoulos. Local transport measurements have been done on ultra-thin MTJ [31] and the currents show large spatial fluctuations, where current peaks at some "hot spots" indicate the existence of pinhole shorts. Experimentally it has been established that a tunneling barrier harboring pinholes exhibits metal-like temperature dependence [32].

Despite the tremendous amount of experimental study on pinhole conducting in MTJs, a theoretical understanding of how pinholes alter the electron transport is lacking. In this work, we present a theoretical study based on a single band tight-binding Hamiltonian and the Landauer formula. The MTJ is modeled in a two terminal geometry: an insulating barrier is sandwiched between two semi-infinite FM leads. The pinhole inside the barrier is modeled as a narrow FM channel, as shown schematically in Fig. 2.1. When magnetization in the FM layers on both sides is anti-parallel, a sharp domain wall is assumed in the pinhole [33].

The Hamiltonian can be written as:

$$H = H_L + H_R + H_B + V,$$

where $H_{L(R)}$ and H_B describe the leads on the left (right) and barrier region, and V is the coupling between leads and barrier. For example, H_L has the form

$$H_L = \sum_{i,\sigma} \epsilon^{\sigma}_{i,L} a^{+}_{i,\sigma,L} a_{i,\sigma,L} - t \sum_{<i,j>,\sigma} (a^{+}_{i,\sigma,L} a_{j,\sigma,L} + h.c.)$$

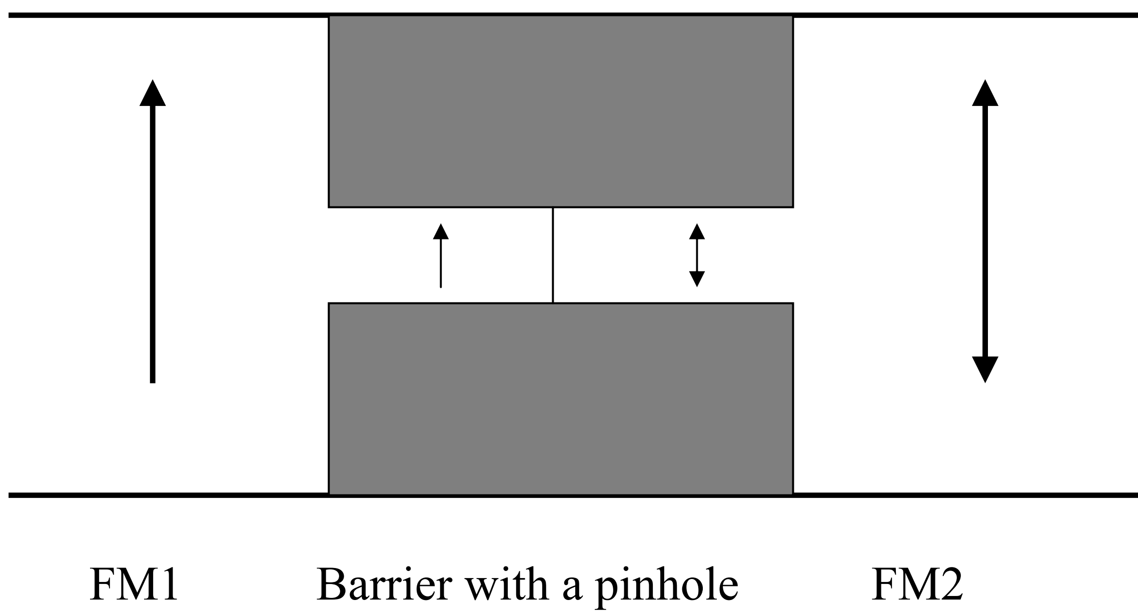

Figure 2.1: Schematic plot of a MTJ harboring a pinhole.

$a^{+}_{i,\sigma,L}(a_{i,\sigma,L})$ is the creation(annihilation) operator on site i with spin σ and $\epsilon^{\sigma}_{i,L}$ is the corresponding onsite energy, with exchange splitting $\epsilon^{\uparrow}_{i,L} - \epsilon^{\downarrow}_{i,L} = 0.5eV$ and hopping integral $t = 0.5eV$. The Hamiltonian in the right electrode and barrier takes a similar form, except that the onsite energy at the barrier region is 3eV to simulate the aluminum-oxide [34]. The Landauer formula will be used to calculate the conductance:

$$G = \frac{e^2}{h} Tr(t^{+}t) = \frac{e^2}{h} \sum_{k_\parallel, k'_\parallel} t_{k_\parallel, k'_\parallel} t^{*}_{k'_\parallel, k_\parallel}$$

The transmission matrix $t_{k_\parallel, k'_\parallel} = i\sqrt{v_{k_\parallel} v_{k'_\parallel}} \mathcal{G}^R(L, k_\parallel; R, k'_\parallel)$ will be calculated from the Green's function $\mathcal{G}^R = \frac{1}{E-H+i0^+}$, which is obtained using the technique introduced in the last section.

We first consider a pinhole which is a single atom chain embedded in a barrier of 1nm (4-atom) thickness. The conductance of various channels as a function of the energy of the incoming electron is calculated. As shown in Fig. 2.2 (a) and (b), the barrier becomes fully transparent, i.e. $G = \frac{e^2}{h}$, at certain energies. The physics for this resonant behavior is as follows: in the pinhole region, the electronic wavefunction is laterally localized because of the confining potential of the barrier. The energy levels of these states are discrete and lie within the conduction band of the electrodes. When the energy of the incoming electron matches the energy of the pinholes states, resonant tunneling happens. The width of each resonant peak is determined by the coupling strength between propagating modes in the leads and the states inside the pinhole.

The pinhole induced resonant tunneling manifests itself through a nonlinear I-V characteristic as in Fig. 2.2 (c). When bias voltage is increased, the electrons with energy inside the bias window all contribute to the current:

$$I = \int_{e_F}^{e_F+V} G(E, V)dE.$$

When the bias window reaches a resonant peak, dI/dV shows a maximum. In principle, one needs to compute the G as a function of energy for each bias self-consistently. But in the low voltage regime, G depends on bias very weakly so it suffices to use the zero bias conductance $G(E, V = 0)$ as in Fig. 2.2 (a) and (b). The MR ratio is defined as

$$MR = \frac{R_{APA} - R_{PA}}{R_{APA}} = \frac{I_{PA} - I_{APA}}{I_{PA}}.$$

The MR exhibit a strong dependence on bias voltage as shown in Fig. 2.2 (d). Clearly, the large variation of the MR is a direct result of the resonant tunneling behavior and the nonlinear I-V relation. A similar resonant magnetoresistance is observed in organic spin valves [35], where the molecule between the FM leads plays the role of the pinhole in our case. Note that our results should be valid only at low bias, where inelastic scattering experienced by the electron is weak. At high bias, magnon induced spin flip scattering [36] will take over and the MR will quickly drop to zero. Interestingly, a bias exceeding 120mV will induce a negative MR ratio leading to an inverse MR effect as in Fig. 2.2 (d). In a recent experiment, negative MR is observed when bias exceeds 225 mV [37]. Our simulation results suggest that the inversion of MR may be attributed to the pinhole induced resonant tunneling.

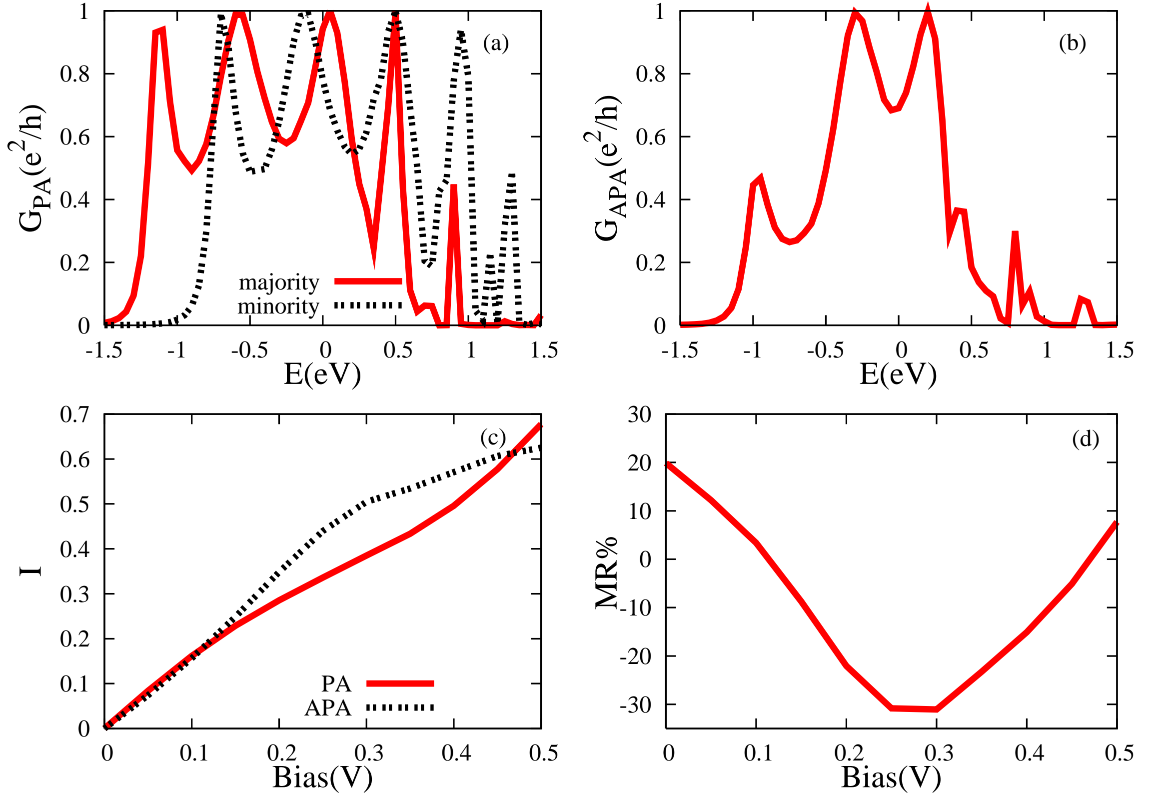

Figure 2.2: Consider a pinhole of one atom in diameter and 1nm (4 atom) long embedded in a MTJ. (a) shows the conductance (measured in $\frac{e^2}{h}$) vs. energy of incoming electron in the parallel alignment (PA) for both majority and minority spin bands; (b) is G vs. E for antiparallel alignment (APA); in (c) nonlinear I-V characteristic is plotted for both PA and APA configuration; (d) shows the MR dependence on bias voltage.

The major mechanism for pinhole formation is the surface roughness of the tunnel barrier. A pinhole appears when the local barrier thickness goes to 0. It is clear that pinholes of various length and width will contribute to the conductance. So in order to properly calculate the magnetoresistance of a rough barrier, we must do an ensemble average over all possible shapes of pinholes. The barrier growth is often modeled as a Poisson process [38], where the local barrier thickness obeys a Poisson distribution. Here we consider only pinholes one atom wide with length satisfying a Poisson distribution to model a rough barrier harboring different pinholes. Although this simplified distribution does not account for every possible shape of pinhole, we believe it is a useful first step that gives some insights into how magnetoresistance is affected by barrier roughness in practice.

Fig. 2.3 (a) and (b) show that the resonant peaks in Fig. 2.2 are smoothed after averaging. As a result, the I-V characteristic is linearized, leading to an ohmic behavior, as in Fig. 2.3 (c). In Fig. 2.3 (d), the averaging erases the oscillation of the MR observed in a single pinhole. The magnitude of the MR is seen to greatly reduce from a perfect MTJ. The reason for this is that the resonant tunneling condition is sensitive to the shape of the pinhole; after averaging the resonant peaks resulting from different pinholes cancel each other in a random manner leading to a smooth and linear I-V curve. Moreover, the averaged resistance for PA and APA are almost identical as seen from Fig. 2.3 (c) which results in a reduced MR. This mechanism provides us some insights on how surface roughness affects the performance of a MTJ

[39].

In practice, a wide pinhole may result from electric break down or be engineered as a current-confined-path [40]. It is therefore important to examine the effects of these very wide pinholes. Owing to the increased width and large number of metallic atoms inside the pinhole, the pinhole density of states is expected to approach the continuum limit and the resonance behavior observed in narrow pinholes should vanish.

Fig. 2.4 shows the MR of a pinhole with lateral dimensions of five atoms by five atoms along with an all-metal GMR sensor. The latter is modeled by directly attaching two FM wires together. Compared to a rough barrier, a wide pinhole will enhance the MR to a magnitude similar to an all-metal GMR sensor. The enhanced MR also suggests the feasibility of the current-confined-path scheme recently proposed [40].

2.3 Surface scattering in nanowires

Nanowires have drawn much interest owing to the extremely broad range of applications in optics [41], magnetism [42, 43, 44] and electronics [45, 46]. Typically, low resistance is crucial. For example, metallic wires functioning as interconnects are basic building blocks in nano-electronic circuits [45] and low resistivity is required to minimize resistive-capacitive (RC) time constants and power consumption. In macroscopic wires, the electronic transport is well described using Ohm's law with resistivity independent of geometric parameters of the wire. Maintaining low resis-

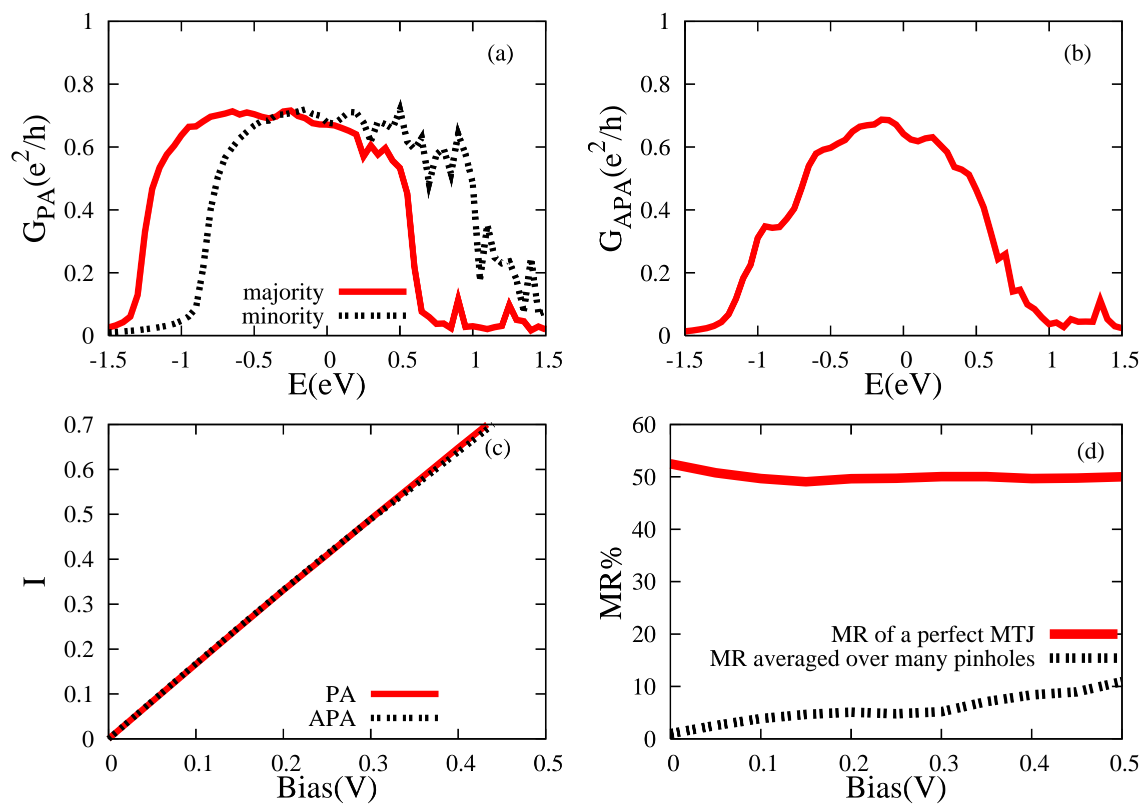

Figure 2.3: Same quantities are plotted as in Fig. 2.2 after averaging over an ensemble of pinholes.

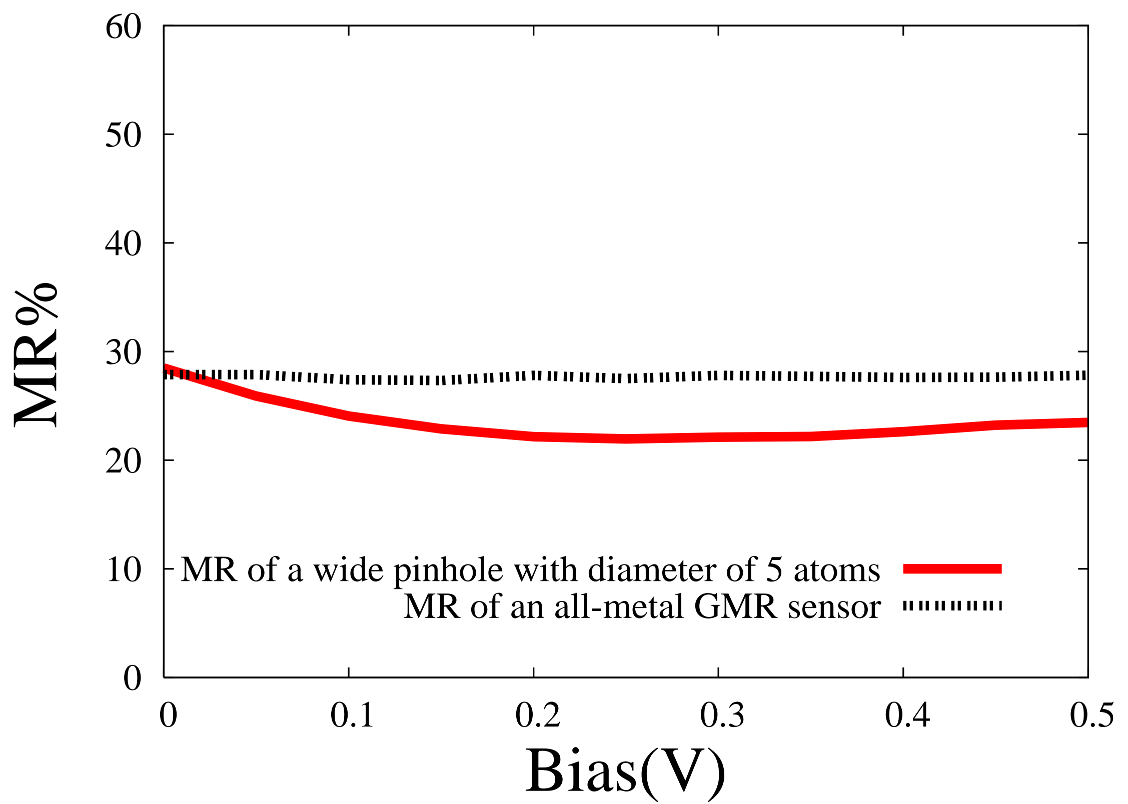

Figure 2.4: The MR of a wide pinhole of 5 atoms in diameter compared with an all-metal GMR spin valve.

tance is challenging because when wires are scaled down to nanometer scale, the MFP significantly decreases due to scattering at grain boundaries and rough surfaces. The resistivity enhancement in thin films caused by an imperfect surface was first studied by Fuchs and Sondheimer [23, 47] semi-classically, based on a phenomenological specularity parameter p, which was later extended by Mayadas and Shatzkes [48] to treat grain boundary scattering. Although these models can successfully fit the experimental data [49, 50], the predictive abilities are limited by their phenomenological nature. In polycrystalline nanowires, grain boundary scattering is the dominant source of resistivity when the mean grain size is comparable to the wire width [49]. Much progress has been made in fabricating single crystalline nanowires to eliminate the grain boundary effect [51]. This leaves surface roughness, which is much harder to control experimentally, as the main source of scattering. It has been experimentally observed that the resistivity of a copper nanowire is about 10 times higher than the bulk value [52]. However, it is still not clear whether this enhancement is mainly due to intrinsic surface scattering or extrinsic factors such as contact resistance or copper oxidation [53]. In this work, we present a quantum mechanical treatment of surface scattering in 3-dimensional (3D) metallic nanowires. With realistic parameters, we will show that surface roughness alone can give rise to a resistivity several times larger than the bulk value.

We consider a segment of 3D wire with length L and square cross section of width W, attached to two semi-infinite leads with equal widths, serving as reservoirs.

The system is modeled by a single band tight binding Hamiltonian with a hopping integral of $t = 1eV$, which is the basic energy scale in this problem, or equivalently a band width of $12eV$. The transport properties of noble metals can be well described by this one band model [5]. The on-site energy for the atoms in the wire is set to be 0 by convention. The metallic wire is embedded into an insulating surrounding environment. The impurity scattering potential Δ is defined to be the difference between the Fermi energy in the wire and the on-site energy of the surrounding insulating atoms. In other words, Δ depends on how the Fermi level of the wire is aligned in the band gap of the insulating material. For instance, for free standing wires in vacuum $\Delta \approx 4.5eV$ which is the work function, for wires grown in a Al_xO template $\Delta \approx 3eV$ as measured in a tunneling experiment [54]. The disorder is introduced by considering a rough interface following a Gaussian distribution with a standard deviation σ.

The Landauer formalism [28, 55, 11] is again employed to calculate the transport coefficients. In the retarded Green's function $\mathcal{G}^R = \frac{1}{E-H-\Sigma_L-\Sigma_R+i0}$, $\Sigma_{L(R)}$ represents the self energy of the left (right) leads. Transmission and reflection coefficients are related to the Green's function by [56]:

$$t_{k_1,k_2} = i\sqrt{v_{k_1}v_{k_2}}\mathcal{G}_{0,k_1;N+1,k_2} \tag{2.4}$$

$$r_{k_1,k_2} = i\sqrt{v_{k_1}v_{k_2}}(\mathcal{G}_{0,k_1;0,k_2} - \frac{\delta_{k_1,k_2}}{iv_{k_1}}) \tag{2.5}$$

with $\mathcal{G}_{m,k_1;n,k_2} \equiv \langle m,k_1|\,\mathcal{G}^R\,|n,k_2\rangle$.

An electronic state in longitudinal layer m with transverse mode k is described

by $|m,k\rangle$. v_k is the velocity of electron determined by the Fermi energy and k. The disordered wire occupies layers from 1 to N and wire length $L = Na$ where $a = 0.25nm$ is the lattice constant. Layer 0 (N+1) is the one in the leads immediately attached to the left (right) of the sample. $\mathcal{G}_{0,k_1;N+1,k_2}$ is numerically evaluated using an efficient recursive Green's function method [56]. In the diffusive transport regime, resistance scales linearly with the wire length which can be described by Ohm's law [57]:

$$R = \frac{\hbar}{e^2}(\frac{1}{M} + \frac{L}{lM}) \equiv \frac{\hbar}{e^2}\frac{1}{T} \tag{2.6}$$

In the above equation M is the number of conducting channels whose subbands cross the Fermi level, l is the elastic MFP and T is the transmission probability. The first term in the bracket of Eq. 2.6 is the contact resistance and the second term comes from the diffusive surface scattering. The MFP is extracted by calculating the resistance as a function of sample length.

When the wire length is below the MFP, transport is ballistic and the conductance takes the quantized value $G = \frac{e^2}{\hbar}M$. As wire length is increased, the system crosses over to the diffusive transport regime where the resistance scales linearly with the wire length and a quantum version of Ohm's law holds. Anderson localization [58] is found at $\xi \approx Ml$, in accordance with well known arguments [59]. The transitions among different transport regimes are shown in Fig. 2.5 for a wire with width $W = 2.5nm$, $\Delta = 4.5eV$ and surface fluctuation $\sigma = 0.25nm$. In the present work we will focus on the diffusive transport regime, which is relevant to most practical applications. The

Fermi energy dependence of the MFP for the same wire is shown in Fig. 2.6. For the energy range of interest, the MFP varies smoothly with the Fermi energy. Hereafter, we will take the Fermi energy to be $0eV$, or at the middle of the band knowing that the resistivity only weakly depends on the exact position of the Fermi level.

Fig. 2.7 displays the elastic MFP as a function of wire width for two surface height deviations $\sigma = 0.25nm$ and $\sigma = 0.125nm$ in the case of strong scattering i.e. $\Delta \gtrsim t = 1eV$. As expected, l decreases when the diameter of the wire goes down. This is due to the fact that in narrow wires, the surface to volume ratio is larger and the surface effect becomes more important. It is also reasonable that the MFP decreases as we increase the surface fluctuation. The MFP is seen to scale linearly with the wire width W. In fact for wires with quadratic cross section, as in our case, the semi-classical Fuchs-Sondheimer model also predicts a linear relation $l = \frac{(1+p)W}{0.897(1-p)}$ [47], where p is the fraction of electrons specularly reflected at the surface. This expression suggests that the slope of the l vs. W curve has a lower limit $\frac{dl}{dW} \geq \frac{1}{0.897}$ when $p = 0$ i.e. all electrons are scattered diffusively at the surface. However, this is violated in our quantum mechanical calculations. For example, in Fig. 2.7(b), when $\Delta = 4.5eV$ we have $\frac{dl}{dW} = 0.69 < \frac{1}{0.897}$. Therefore, the calculated MFP is smaller than the lowest value allowed by FS model. The discrepancy can be attributed to the fact that, for large impurity potential Δ, electrons have a larger chance of being reflected rather than being scattered equally to all directions as assumed in FS model. Also, the quantum coherent backscattering, which is neglected in the semi-classical model,

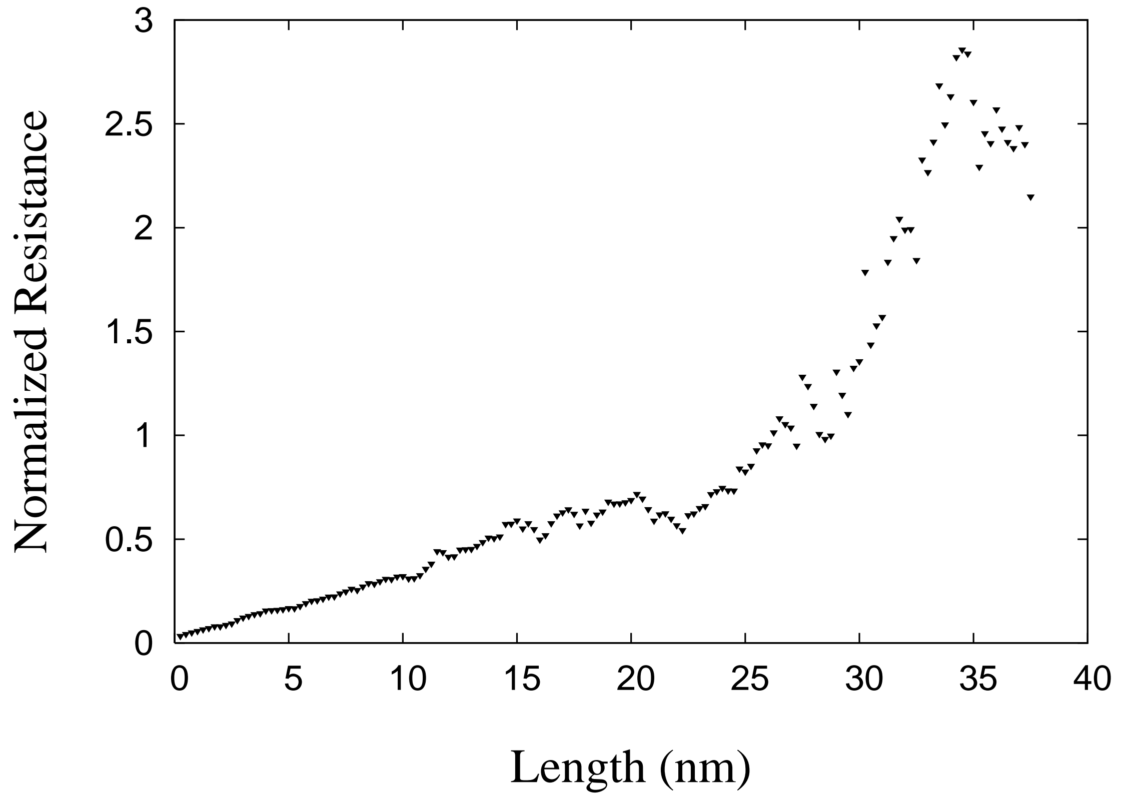

Figure 2.5: Sample calculation of normalized resistance $R/(\frac{\hbar}{e^2})$ as a function of length for a 3D wire of $2.5nm$ wide. MFP $l \approx 0.46nm$ is obtained in the linear regime. The onset of localization occurs around $L \approx Ml = 30nm$.

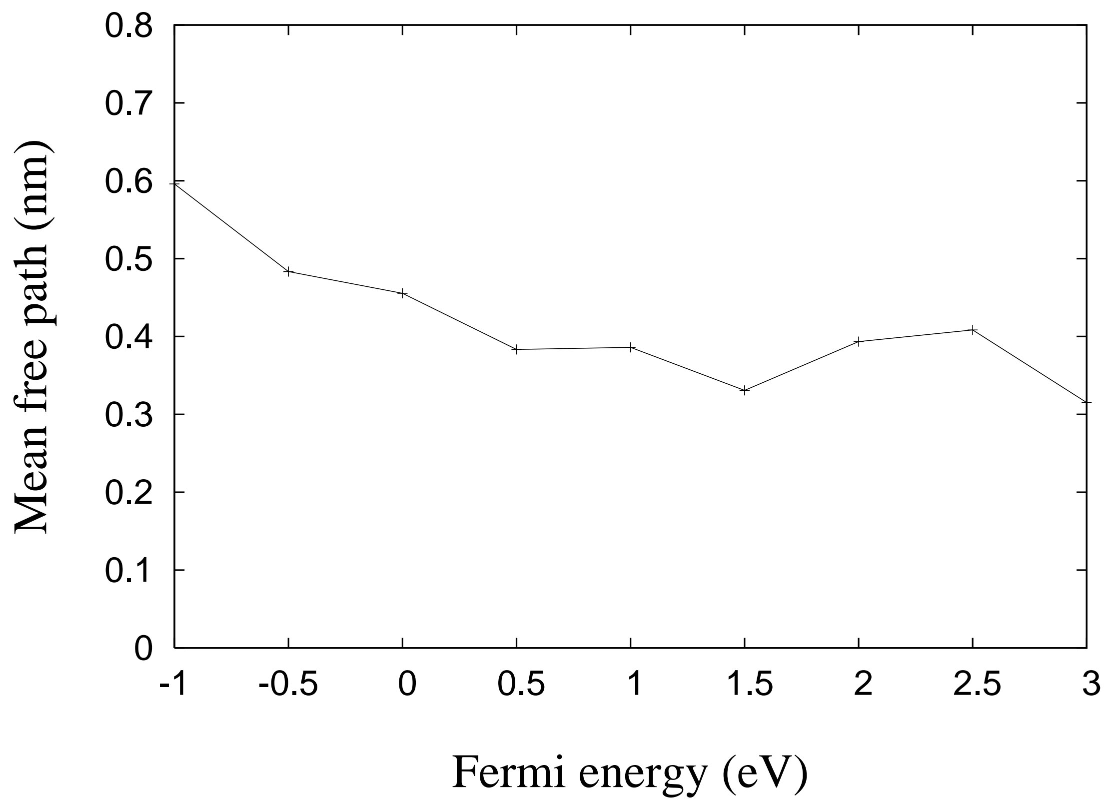

Figure 2.6: The MFP as a function of Fermi energy.

may also play a role [60].

For weak scattering $\Delta \lesssim 1eV$, the MFP increases with W in an oscillatory manner, as shown in Fig. 2.8 for $\Delta = 0.5eV$, which is also observed by Todorov for bulk disorder [57]. This behavior is beyond the scope of the FS model but, as we show below, it can be produced by perturbatively expanding the Green's function: the expansion is equivalent to a Born approximation. To make progress analytically, we consider a slightly different model where the impurity atom is randomly introduced in the surface layer with a probability P. Formally the Hamiltonian is written as $H = H_0 + V$. The first term H_0 represents a perfect wire and the term $V = \sum\limits_{i,s} \Delta_{i,s} |i,s\rangle \langle i,s|$ describes the impurities on the surface, where i and s label the longitudinal layer number and the transverse coordinates on the surface respectively. $\Delta_{i,s}$ is impurity potential Δ with probability P or 0 otherwise. It is assumed that the impurities are independently distributed on the surface i.e. $\langle \Delta_{i,s}\Delta_{j,s'} \rangle = P^2\Delta^2 + \delta_{i,j}\delta_{s,s'}(P\Delta^2 - P^2\Delta^2)$. The reflection rate is calculated by expanding the Green's function to first order in V using Dyson's equation:

$$\mathcal{G}_{0,k;0,k'} = \mathcal{G}^0_{0,k;0,k'} + \sum_{i=1}^{N} \mathcal{G}^0_{0,k;i,k} V^i_{k,k'} \mathcal{G}^0_{i,k';0,k'} \tag{2.7}$$

Here $V^i_{k,k'} = \sum\limits_{s} \varphi^*_k(s)\varphi_{k'}(s)\Delta_{i,s}$ is the matrix element for inter-subband scattering that occurs in layer i which is essential for reflection. Therefore, according to Eq. 2.5 and using $iv_k\mathcal{G}^0_{0,k;0,k'} = \delta_{k,k'}$, the reflection amplitude $r_{k,k'} = i\sum\limits_{i} \sqrt{v_k v_{k'}}\mathcal{G}^0_{0,k;i,k} V^i_{k,k'} \mathcal{G}^0_{i,k';0,k'}$. This expression equals 0, unless both subbands k, k' cross the Fermi level in which case $\langle |r_{k,k'}|^2 \rangle = \frac{1}{v_k v_{k'}}(\sum\limits_{i} \langle V^i_{k,k'} V^{i*}_{k,k'} \rangle + \sum\limits_{i \neq j} \langle V^i_{k,k'} V^{j*}_{k,k'} \rangle)$, where $\langle \cdots \rangle$ stands for ensemble

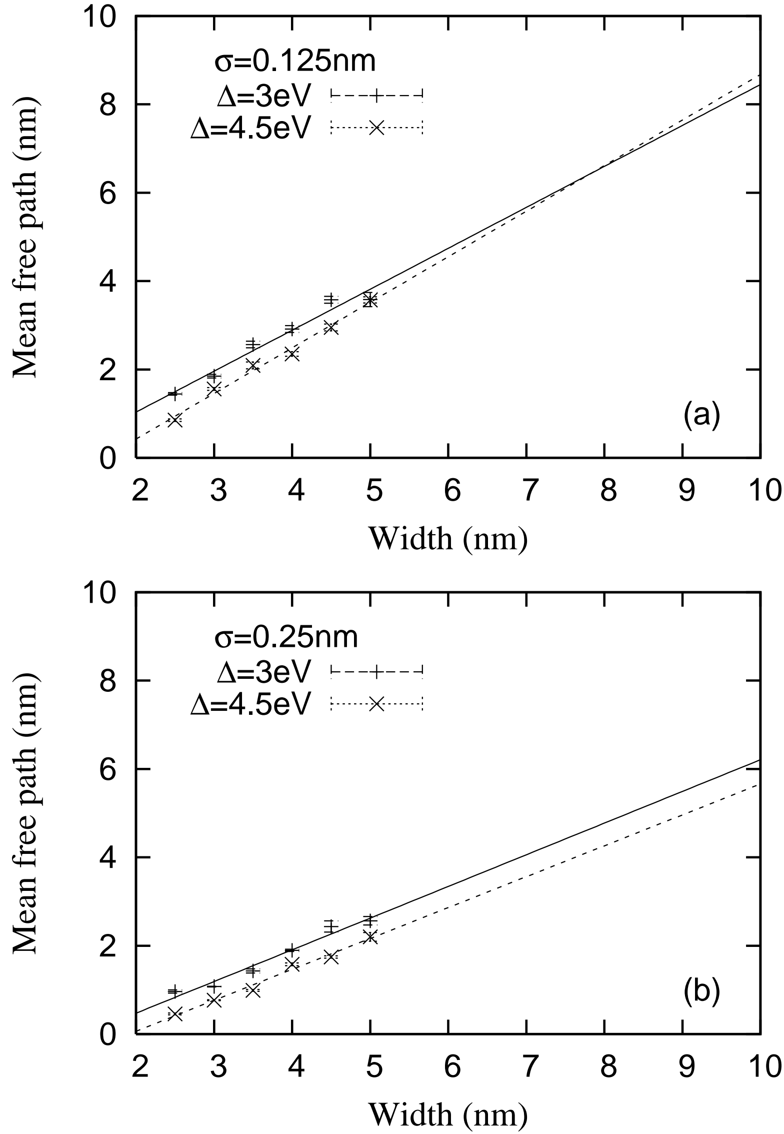

Figure 2.7: MFP as a function of wire width in the strong scattering regime ($\Delta > 1eV$) for two different surface fluctuations: $\sigma = 0.125nm$ in (a) and $\sigma = 0.25nm$ in (b). The solid and dashed lines are the linear fit to the data.

average over disorder. In order to calculate the MFP, only terms linear in the wire length L are retained which implies $\left\langle |r_{k,k'}|^2 \right\rangle = L \sum_s P(1-P)\Delta^2 \frac{|\varphi_k(s)|^2 |\varphi_{k'}(s)|^2}{v_k v_{k'}}$. By definition, the transmission probability $T = M - \sum_{k,k'} \left\langle |r_{k,k'}|^2 \right\rangle$. In the weak scattering limit this gives $\frac{1}{T} \approx \frac{1}{M} + \frac{\sum_{k,k'} \left\langle |r_{k,k'}|^2 \right\rangle}{M^2}$. Comparing to Eq. 2.6 an analytical expression for the MFP is obtained:

$$l = \frac{M}{P(1-P)\Delta^2 \sum_{s,k,k'} \frac{|\varphi_k(s)|^2 |\varphi_{k'}(s)|^2}{v_k v_{k'}}}. \tag{2.8}$$

The analytical expression Eq. 2.8 agrees well with the exact numerical results as shown in Fig. 2.8 for the case $\Delta = 0.5eV$, $P = 0.1$. Therefore the oscillatory behavior of the MFP absent in the FS model is a quantum size effect caused by quantum interference. In addition to the oscillation, the MFP grows roughly linearly with wire width which can be shown using the following simple scaling relations. Notice that $M \propto W^2$, $\sum_{s,k,k'} \propto W^5$ and $|\varphi_k(s)|^2 \propto \frac{1}{W^2}$, which comes from the renormalization constant in the wavefunction: therefore, $l \propto W$.

To study the effects of environment surrounding the nanowire, we calculate MFP as a function of the impurity potential Δ as shown in Fig. 2.9. At weak scattering $\Delta \lesssim 1eV$, $l \propto \frac{1}{\Delta^2}$ in agreement with Eq. 2.8. For strong scattering the perturbation theory breaks down and l, instead of going to zero, approaches a constant. The results suggest that MFP can be increased when the nanowire is surrounded by insulating materials with a narrow band gap.

Although nanowires wider than $5nm$ are beyond our current computational ability,

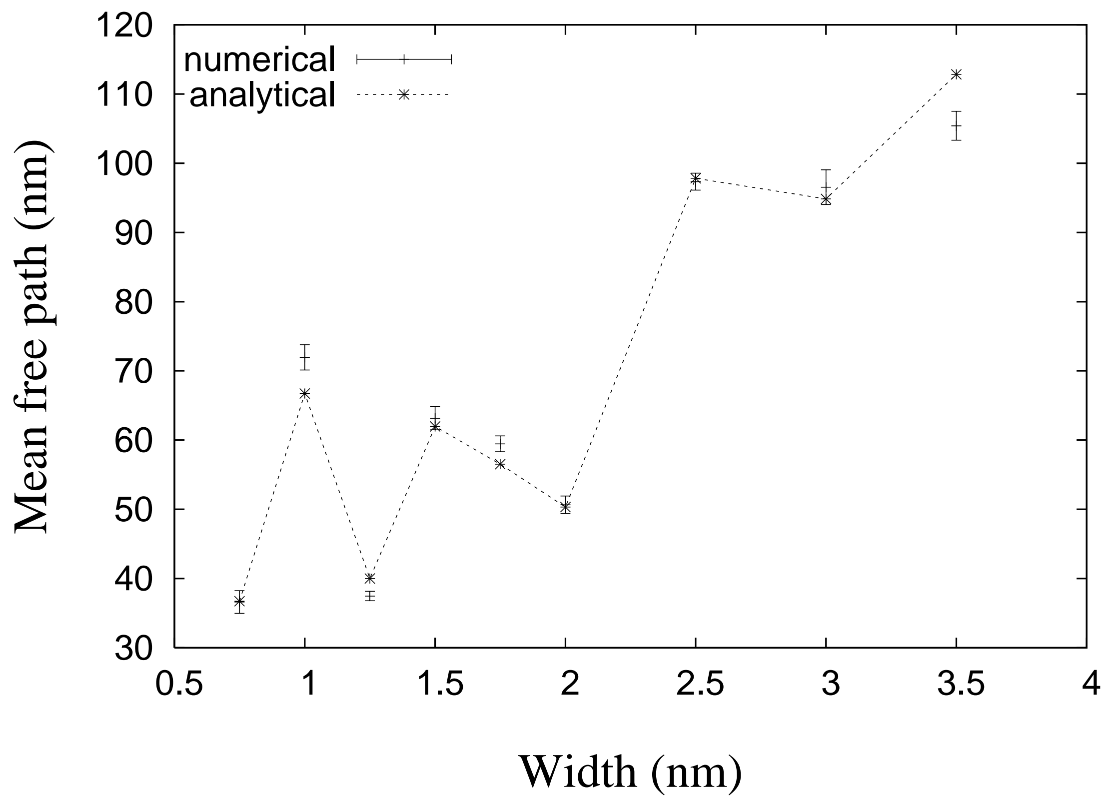

Figure 2.8: MFP vs. width in the weak scattering regime $\Delta = 0.5eV$ as compared to the analytical results in Eq. 2.8.

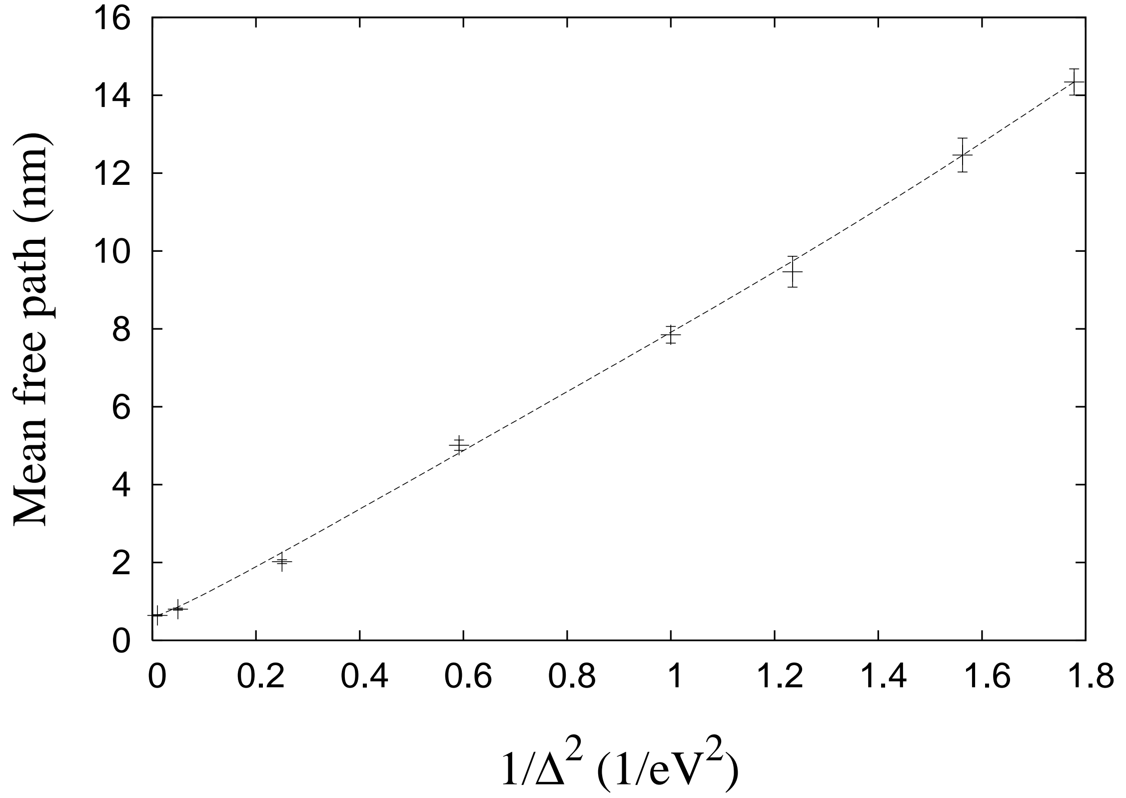

Figure 2.9: MFP's dependence on impurity potential Δ in a 12 atom by 12 atom wire. For weak scattering ($\Delta \lesssim 1eV$), $l \propto \frac{1}{\Delta^2}$ as expected from Eq. 2.8. As Δ increases, the MFP approaches a nonzero constant.

we have observed that MFP scales linearly with the wire diameter, which is also supported by the analytical theory. So MFP of nanowires with larger sizes can be obtained by a linear extrapolation based on results in Fig. 2.7, as listed in table below. In contrast, the bulk MFPs for noble metals at room temperature are $l_{Au} = 40.9nm$, $l_{Ag} = 55.6nm$ and $l_{Cu} = 43.1nm$ [5]. For nanowires surrounded by vacuum i.e. $\Delta = 4.5eV$, it is seen that for a nanowire of about $20nm$ wide, the MFP caused by surface scattering alone is several times larger than the bulk value, even for very smooth surface with standard deviation of roughness equal to 1 atomic spacing. More typical roughness will generate even larger effects.

Wire width (nm)	10	20	40	60	80
$\sigma = 0.25nm$	5.6	12.7	26.6	40.6	54.6
$\sigma = 0.125nm$	8.7	19.0	39.6	60.2	80.8

2.4 Surface scattering in magnetic nanostructures

Scattering due to suface roughness plays an important role in magnetoresistive devices. In the case of an MTJ, it is crucial to have a ultrasmooth interface between the electrode and magnetic layer. Experimentally, it has been observed that the MR inversely depends on barrier thickness and the roughness of the interface between barrier and ferromagnetic layer [61].

In this section, we attempt to understand such phenomena by carrying out quantum transport calculations for a MTJ with a rough interface. In Fig. 2.10, we plot

the MR as a function of RA product for barriers with different roughness, where the interface is assumed to follow a Gaussian distribution with standard deviation σ. For a smooth barrier ($\sigma = 0$) the MR rapidly increases with the RA, or equivalently, barrier thickness, in a fashion that is similar to a MgO based MTJ [11]. In Fig. 2.10, we plot the MR as a function of RA product for barriers with different roughness, where the interface is assumed to follow a Gaussian distribution with standard deviation . Experimentally, however, such rapid increase of MR is not observed [62]. Instead, in these experiments, MR increases with RA moderately and tends to saturate for thick barriers. This behavior can be qualitatively explained by including surface roughness into the calculation, as seen from Fig. 2.10.

As a special case, notch shaped roughness can form in the barrier (see Fig. 2.11 (a)), where the local barrier thickness is reduced yet there is no pinhole and the barrier thickness is 2 nm. When notches form, they tend to dominate the electron transport process, because they provide a short cut for current. Therefore, it is important to investigate how they affect the behavior of the MTJ. As shown in Fig. 2.11 (b), the MR ratio drops with the notch depth. This is because, for a deeper notch, the electron is effectively tunneling through a thinner barrier, which leads to a reduced MR as observed in Fig. 2.11. The RA product drops significantly with increasing notch depth, as displayed in Fig. 2.11 (c). We note that even without forming pinholes, roughness induced structures can dramatically change the electric and magnetic properties of the MTJ.

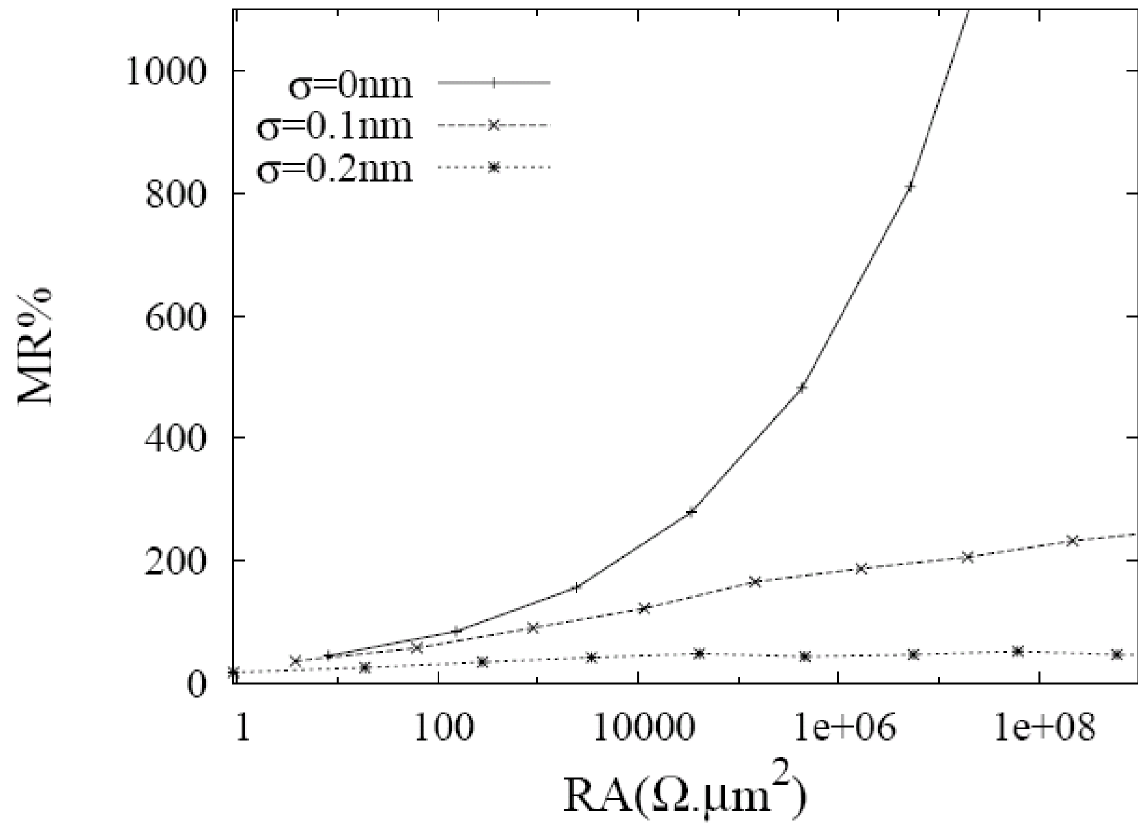

Figure 2.10: Magnetoresistance as a function of resistance-area product (by varying barrier thickness) for different surface roughness.

Magnetoresistive devices based on magnetic nanowires have been intensively studied in recent years [63] due to the need for a nanometer-scale magnetoresistance (MR) devices in spintronic and high density magnetic recording applications. We will extend our metallic nanowire model in the last section to the magnetic case and study the influence of surface roughness on MR. In a nanowire based GMR device, since surface induced scattering is spin independent and does not contribute to the spin dependent resistance, we expect the magnetoresistance is reduced in these rough wires. In Fig. 2.12, resistance of parallel and anti-parallel alignment both increase linearly with wire length, while the magnetoresistance drops, for wires with width of 6 atoms.

When a MTJ structure is built in a nanowire, we expect that the surface roughness does not play as big a role as in the GMR case, because the barrier resistance dominates the wire resistance. Indeed, as shown in Fig. 2.13 (b), the MR does not drop with increasing wire length, where the wire width is 6 atoms with a roughness of $\sigma = 0.4nm$. However, it is interesting to note that the resistance of the device dropped after attaching leads with surface roughness, as shown in Fig. 2.13 (a), where the zero length case corresponds to a MTJ with no rough leads. This unexpected reduction of resistance is a quantum effect and can be explained by coherently combining the scattering matrix of the rough leads and barrier:

$$T_{12} = \frac{T_1 T_2}{1 - 2\sqrt{R_1 R_2}\cos\theta + R_1 R_2}, \tag{2.9}$$

where $T_1(T_2)$ and $R_1(R_2)$ are the transmission and reflection probability of the rough

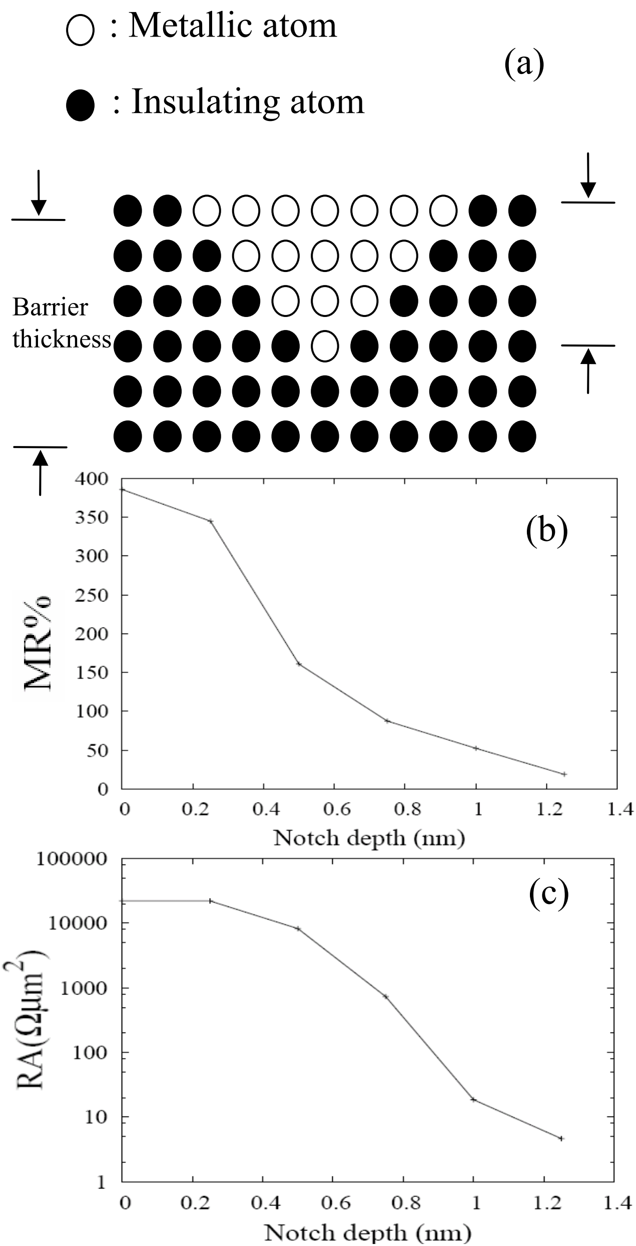

Figure 2.11: (a). Schematic view of a barrier with a notch. (b) and (c), MR ratio and RA product as function of notch depth.

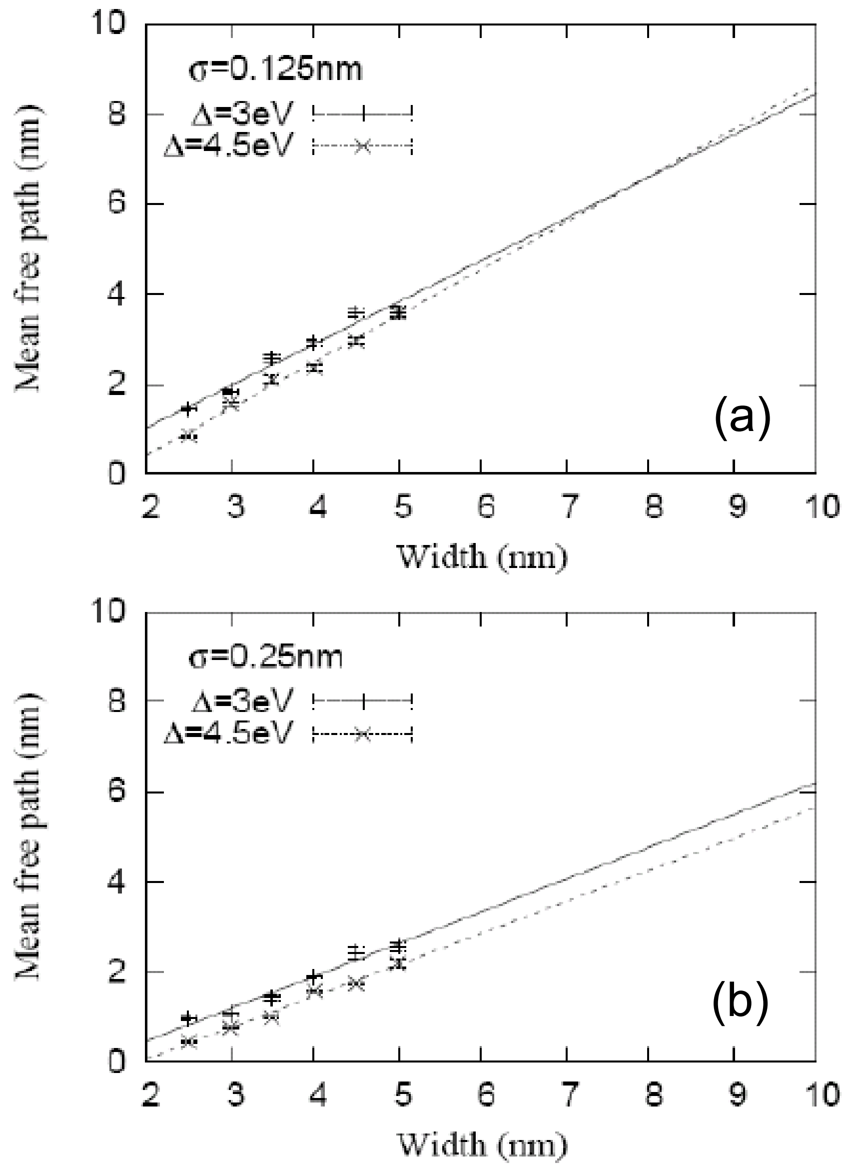

Figure 2.12: (a). Resistance vs. wire length for parallel alignment (PA) and anti-parallel alignment (APA) for a nanowire-based GMR device with two different roughnesses. (b). Magnetoresistance as a function of wire length.

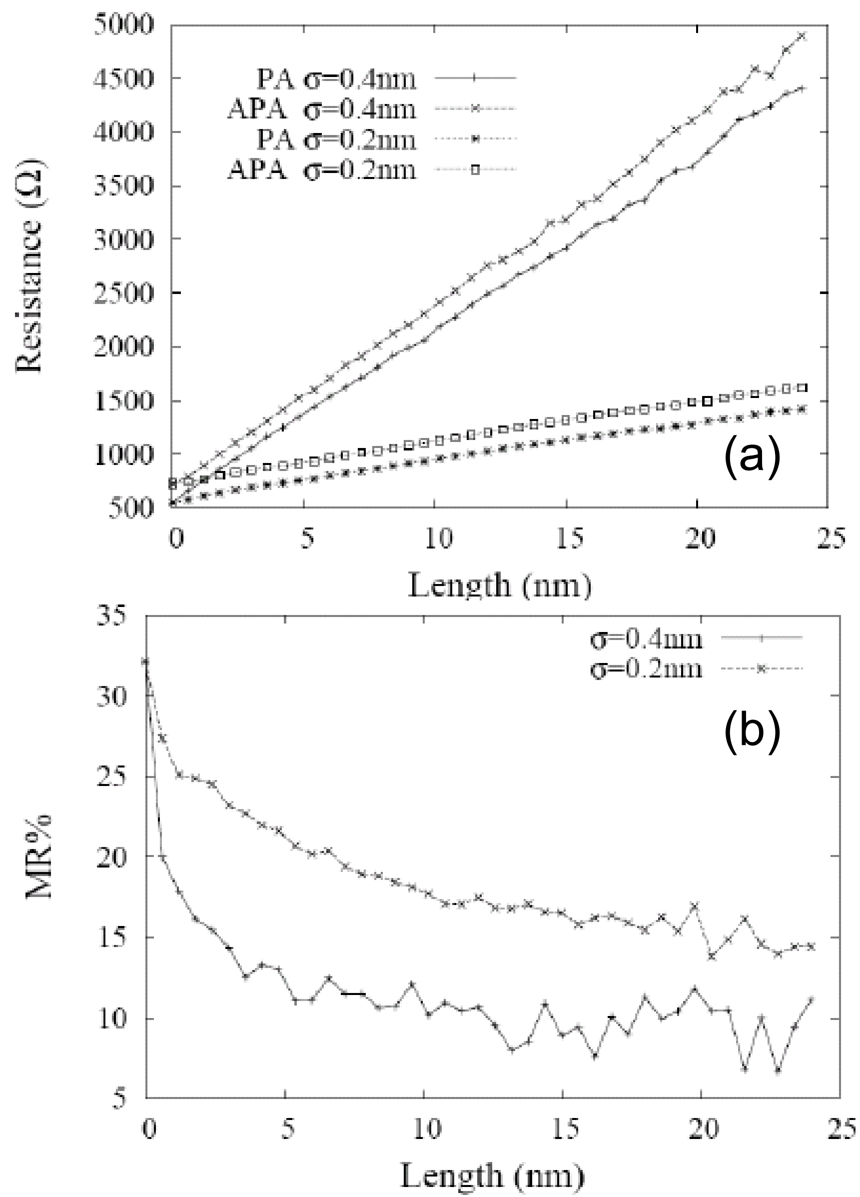

Figure 2.13: (a). Resistance vs. wire length for parallel and anti-parallel alignment for nanowire based GMR device. (b). Magnetoresistance as a function of wire length.

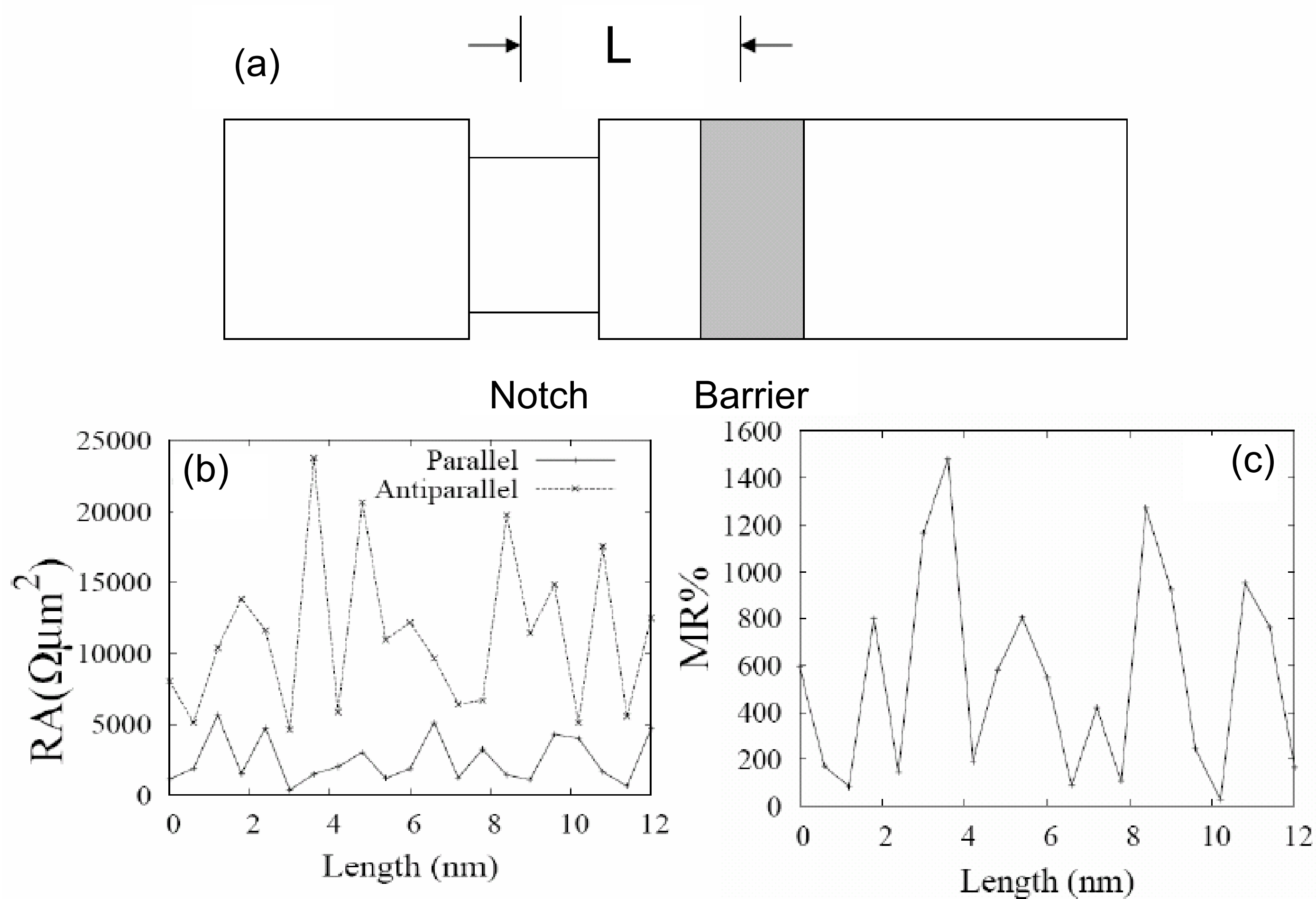

Figure 2.14: (a): Schematic plot of a fabricated notch in front of the barrier. (b) The resistance as a function of notch-barrier separation L. (c) Magnetoresistance vs L.

leads (barrier). The angle θ is the phase accumulated by the electron traveling between leads and barrier. Since the leads are directly attached to the barrier, we assume $\theta \approx 0$. It can be readily seen from Eq. 2.9 that for $T_1 \approx 1$ and $R_2 \approx 1$, thus explaining the reduction of resistance observed in Fig. 2.13 (a).

The resistance reduction is attractive for the application of MTJ devices. We can engineer a structure that reduces the resistance of the MTJ based on the coherent transport of electrons as described above. As an example, a notch is fabricated in the nanowire at a distance L from the barrier as shown in Fig. 2.14(a), where atoms on the surface layer are replaced with insulating atoms. The wire width is set to be 6 atoms. The phase θ accumulated between barrier and notch varies with distance D. Therefore, the resistance exhibits an oscillatory behavior as a function of L (Fig. 2.14(b)). At the proper distance (3nm), it is possible to increase MR while simultaneously decreasing resistance (Fig. 2.14(c)).

2.5 Conclusions

In this chapter, we investigated the electron transport in several magnetic nanostructures, with emphasis on the effect of roughness induced scattering. A quantum mechanical approach based on the Landauer formalism and a Green's function technique is used to calculate the spin resolved conductance. A tight-binding Hamiltonian is used to describe the electronic structure.

Pinholes in magnetoresistive devices such as MTJs and spin valves were studied.

It is shown that a narrow pinhole, e.g. 1 atom width, embedded in a MTJ induces resonant tunneling behavior, resulting in an oscillating MR as a function of bias voltage. A negative MR is found when the bias exceeds 120 mV, suggesting the inverse MR effect observed in a recent experiment [37] may be attributed to pinhole induced resonant tunneling. We then model a MTJ with a rough surface by considering an ensemble of pinholes with different shapes. After averaging, the oscillation of MR seen in the single pinhole case is smoothed and the magnitude of the MR ratio is greatly reduced compared with a perfect MTJ, which explains how surface roughness diminishes the MR. Finally, we investigate a wide pinhole, e.g. 5 atoms across, motivated by the experimental efforts on current-confined-path GMR films. It is found that a large pinhole produces an enhanced MR ratio with a value similar to an all-metal GMR.

The effects of surface scattering on electronic transport in metallic nanowires are also studied. In the weak scattering regime, the MFP grows in an oscillatory manner as a function of width which is beyond the scope of the classical model but is well explained by a perturbation theory. It is found that the MFP scales linearly with the width W for strong scattering. It is shown that the MFP depends inversely on impurity potential Δ^2 for weak scattering as expected from the perturbation result. Most interestingly, for very narrow wires (width below $20nm$), the rough surface becomes dominant and gives rise to a resistivity several times larger than the bulk value. This may account for the resistivity enhancement observed in experiment [52]

and, potentially, greatly impacts RC time constants and power consumption in future electronic devices. Since this scattering is spin-independent, this leads to a reduced MR. In particular, MR is found to decrease in longer or narrower wires.

Chapter 3

Exchange assisted spin torque switching

3.1 Introduction

Angular momentum transferred from a spin-polarized electric current to the local magnetic moment gives rise to a spin transfer torque (STT) and opens up new routes for electrical manipulation of magnetization. Due to its applications in potential spintronic devices, the effect has stimulated many experimental and theoretical studies over the last decade [12, 13]. With sufficient current, it has been shown that current induced magnetization switching (CIMS) can happen in spin valve and MTJ devices. CIMS has stimulated much interest not only because of its important scientific merits but also numerous potential applications. As discussed in the first

chapter, one promising application of CIMS is the magnetoresistive random access memory (MRAM). Compared to other forms of memory, such as dynamic random access memory (DRAM), electrically erasable programmable read-only memory (EEPROM), flash memory etc., the chief advantage of the MRAM over its competitors mentioned above is its ability to combine various appealing attributes into one single memory solution, such as non-volatility, low power consumption and speed. The potential for MRAM to replace existing technologies leads to intensive research on the topic.

The CIMS offers many advantages over traditional field switching including simplification of design and scaling ability for high density memory. To integrate the existing semiconductor technologies, it is crucial to lower the switching current density. For the in plane geometry, the switching current is dominated by the demagnetization field, which does not contribute to thermal stability. Materials with a sufficient perpendicular anisotropy can be used to pull the magnetization out of plane, which reduces the switching current without sacrificing thermal stability. On the other hand, with the increase of storage density, it is expected that high anisotropy material will be used to make the bit state stable against thermal fluctuations, which, unfortunately, requires a proportionally high switching current density.

There have been several proposals aiming to lower the switching current. Some of these methods are based on increasing the spin torque efficiency, such as by inserting a Ru layer between free layer and electrode [20] or using high quality tunnel barrier

[64]. Another approach is to use a nano-current channel structure to boost the local current density while reduce the overall switching current [65].

3.2 Exchange assisted switching

So far most of the experiments on CIMS uses a single magnetic layer as the free layer. Here we propose a composite free layer consisting several exchange coupled magnetic layers, with graded anisotropy. The idea is to employ the soft layer (low anisotropy) to assist the switching of the hard layer. A similar structure has been studied to lower the switching field in the context of perpendicular magnetic recording [66]. However, it is important to note that the switching mechanism of CIMS is fundamentally different from that of field switching, as discussed in the Chapter 1.

The proposed structure is shown in Fig. 3.1, that contains a current source, a fixed layer to polarize the current, a recording layer and an assisting layer with lower anisotropy. The assisting layer is exchanged coupled to the recording layer through a metallic spacer and is separated from the fixed layer by a tunnel barrier. We consider the case where each layer has a perpendicular anisotropy $K_\perp$ that is larger than the shape anisotropy $4\pi M_S$ so that the magnetization rests out of plane in equilibrium and the effective anisotropy is $K_\perp - 4\pi M_S$.

The free energy of exchange coupled soft and hard layers is

$$E = -K_S(\vec{m}_S \cdot \hat{z})^2 - K_H(\vec{m}_H \cdot \hat{z})^2 - J\vec{m}_H \cdot \vec{m}_S, \tag{3.1}$$

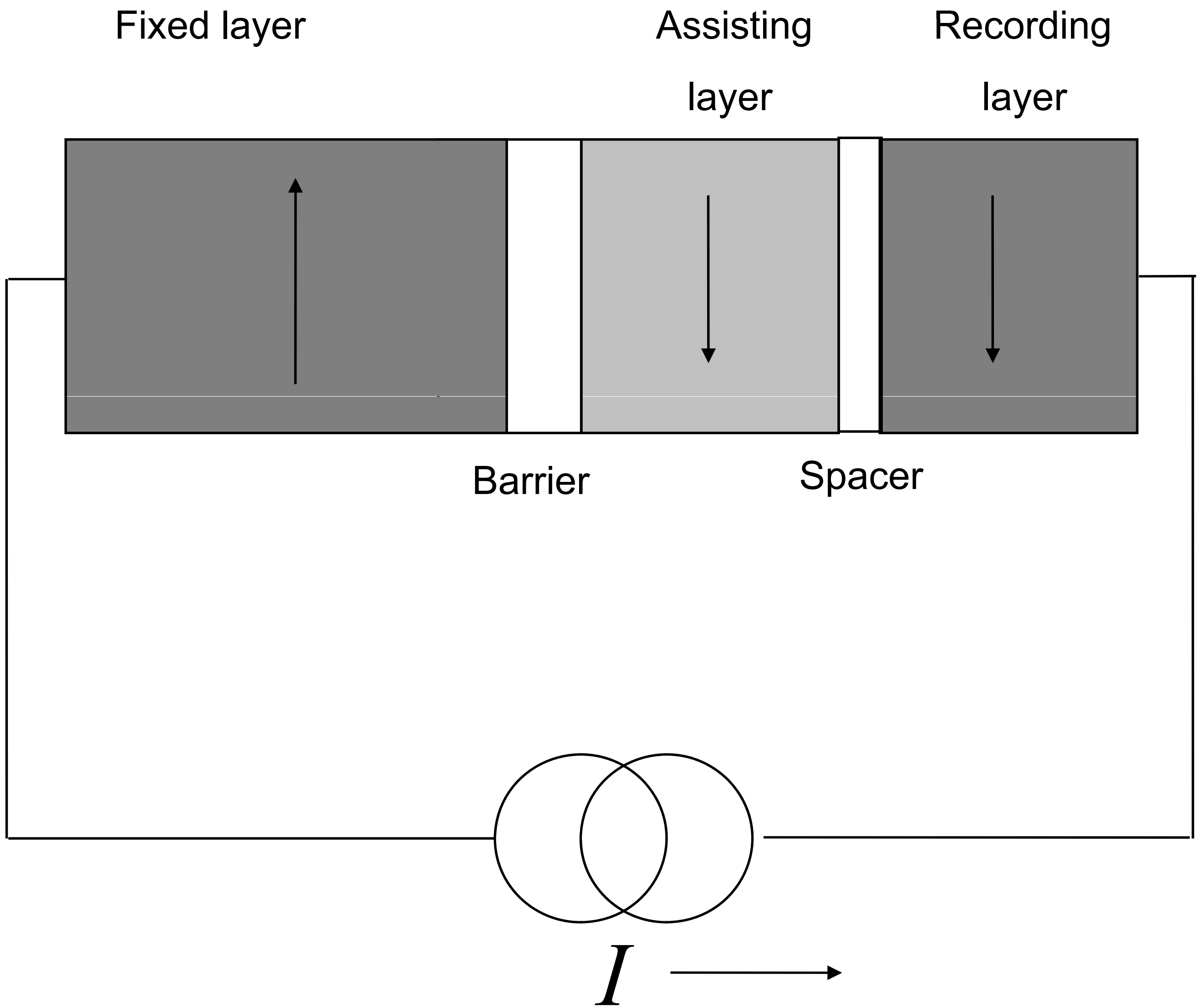

Figure 3.1: The exchange coupled composite structure proposed to reduce switching current.

where $K_S = K_{S\perp} - 4\pi M_S$ and $K_H = K_{H\perp} - 4\pi M_S$ are the uniaxial anisotropy constants for soft and hard layer, respectively, $\hat{z}$ is the easy axis direction, J is the exchange coupling constant between layers, m_S and m_H are unit vectors pointing along the two layers.

The dynamics are modeled with the Landau-Lifshitz-Gilbert equation with a spin torque term:

$$\begin{aligned} \frac{\partial \vec{m}_S}{\partial t} &= -\gamma \vec{m}_S \times \vec{H}_{eff} - \alpha_S \gamma \vec{m}_S \times (\vec{m}_S \times \vec{H}_{eff}) + \gamma \frac{P\hbar j}{edM_S} \vec{m}_S \times (\vec{m}_S \times \hat{p}), \\ \frac{\partial \vec{m}_H}{\partial t} &= -\gamma \vec{m}_H \times \vec{H}_{eff} - \alpha_H \gamma \vec{m}_H \times (\vec{m}_H \times \vec{H}_{eff}), \end{aligned} \tag{3.2}$$

where $\hat{p}$ is the polarization direction of the spin current coming out of the fixed layer, P is the spin torque efficiency, d is the soft layer thickness and j is the current density. In the absence of soft layer, the switching current for a single hard layer is $j_{c0} = \frac{\alpha_H ed}{P\hbar} K_H$.

To study the different dynamic behavior of the coupled double-layer system, we calculate the dynamic phase diagram by varying exchange J and current density j. For simplicity, J and j are normalized by the hard layer anisotropy K_H and j_{c0}, respectively. As shown in Fig. 3.2, there are 4 different regimes. In regime 1, neither the hard or the soft layer switches, corresponding to the strong coupling limit discussed previously. In regime 3, only the soft layer switches, corresponding to the weak coupling limit. Regime 2 is an intermediate state with steady precession of magnetization. Here we are mainly interested in regime 4, where both layers switch. It can be readily seen that for a exchange of about $J/K \approx 0.3$, the switching current

can be reduced to about 15% of that of direct switching j_{c0}.

To fully utilize this structure, we can incorporate more assisting layers with graded anisotropy, as displayed in Fig. 3.3. The switching current depends on how the anisotropy varies layer by layer.

The switching current for different numbers of soft assisting layers ranging from 1 to 5 is shown in Fig. 3.4. Again, we have assumed all the soft layers have damping constant of 0.01. From Fig. 3.4, we observe that the minimal switching current drops as we add more soft layers and the optimal exchange strength increases. For 5 soft layers, the switching current can be lowered by a factor of about 30. Other methods based on increasing spin torque efficiency typically reduce j_c by a factor of around 3. This is because in a normal ferromagnet such as permalloy, the spin torque efficiency is about 0.3, while the maximal efficiency is 1, which fundamentally limits the reduction capability. The approach studied here, however, does not suffer from this limitation and is based on a dynamic effect. The switching mechanism can be understood using the concept of a domain wall. In the first few layers with lowest anisotropy, it is easy to switch them in the presence of spin current. Once they are switched, a domain wall forms. Driven by the exchange interaction, the domain wall propagates down the structure and eventually switches the hardest layer. Since it is well known that domain wall propagation is much less energetically expensive than direct coherent rotation, a reduction of switching current can be achieved.

So far, we have assumed the soft layers have a low damping constant $\alpha_S = 0.01$

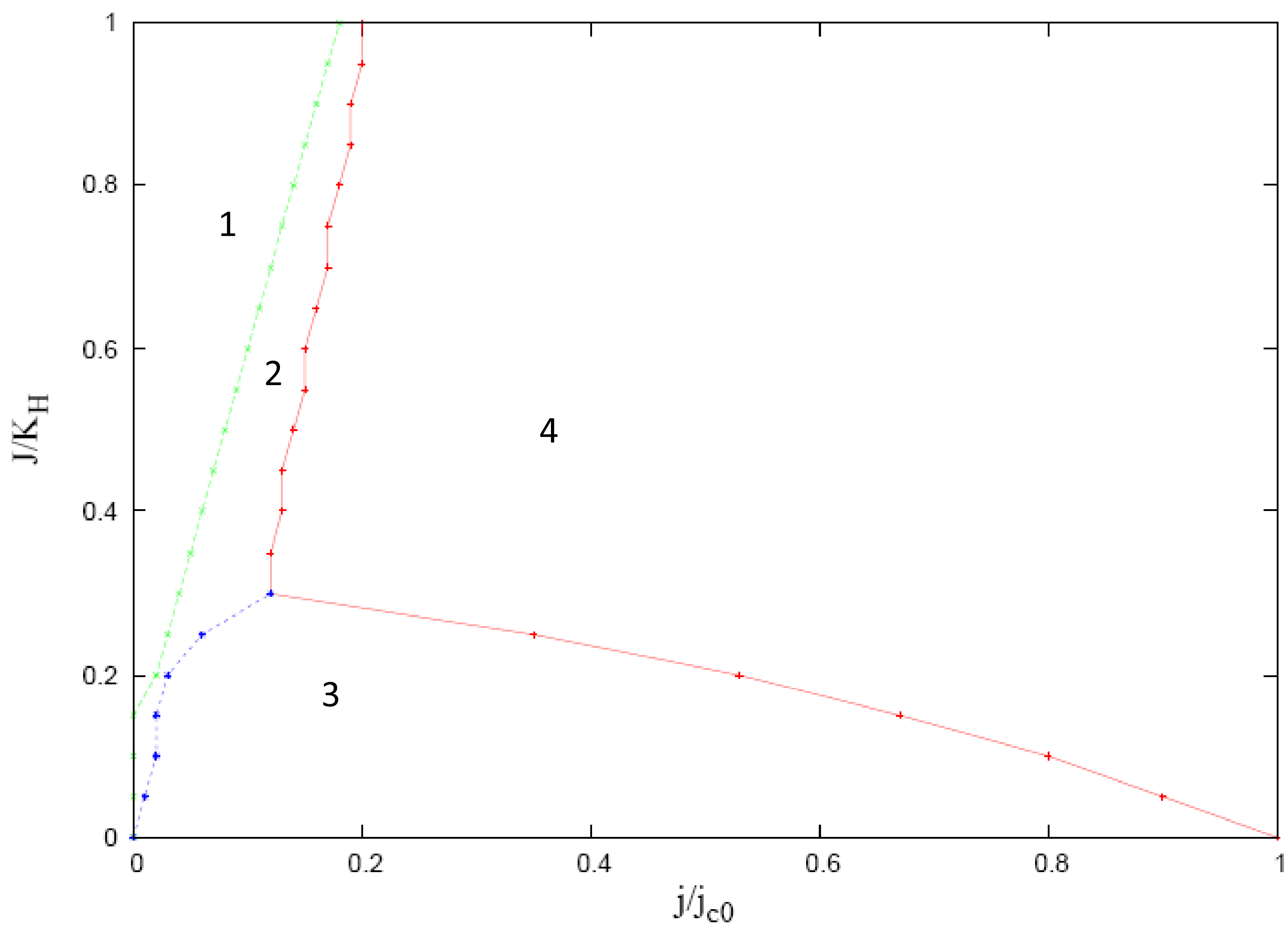

Figure 3.2: The dynamic phase diagram of the double layer structure.

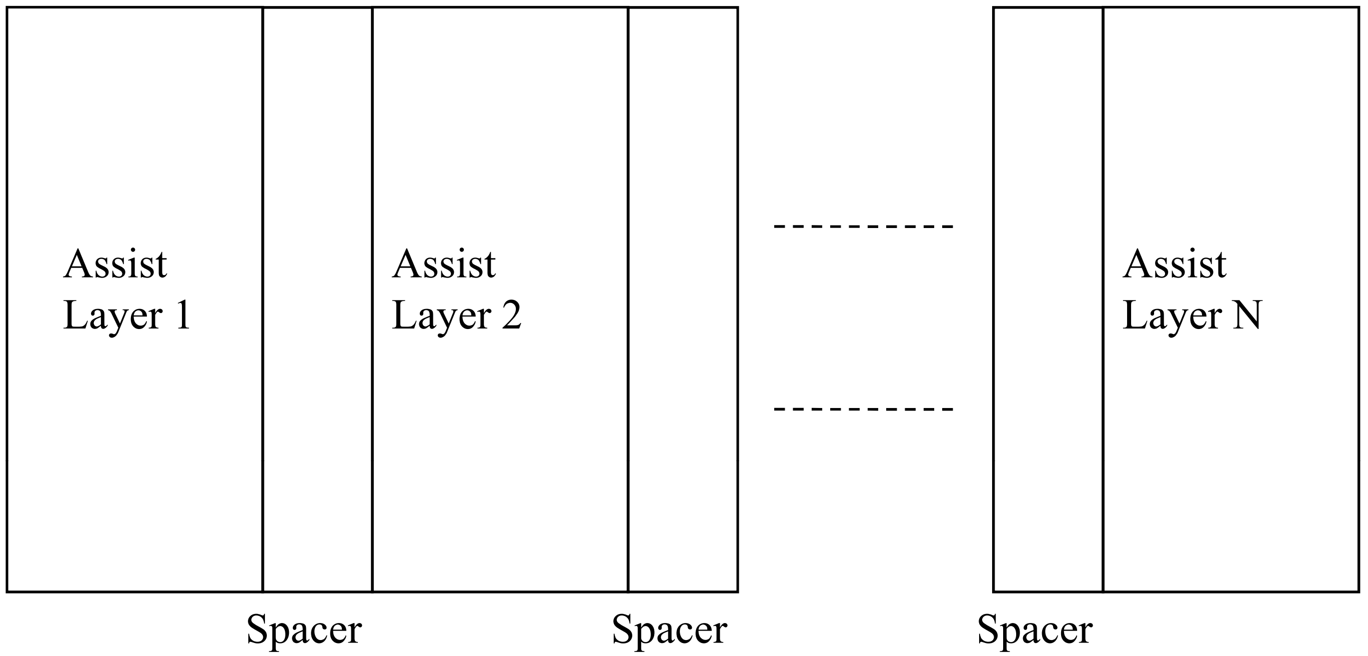

Figure 3.3: The composite structure consisting multiple soft assisting layers with graded anisotropy.

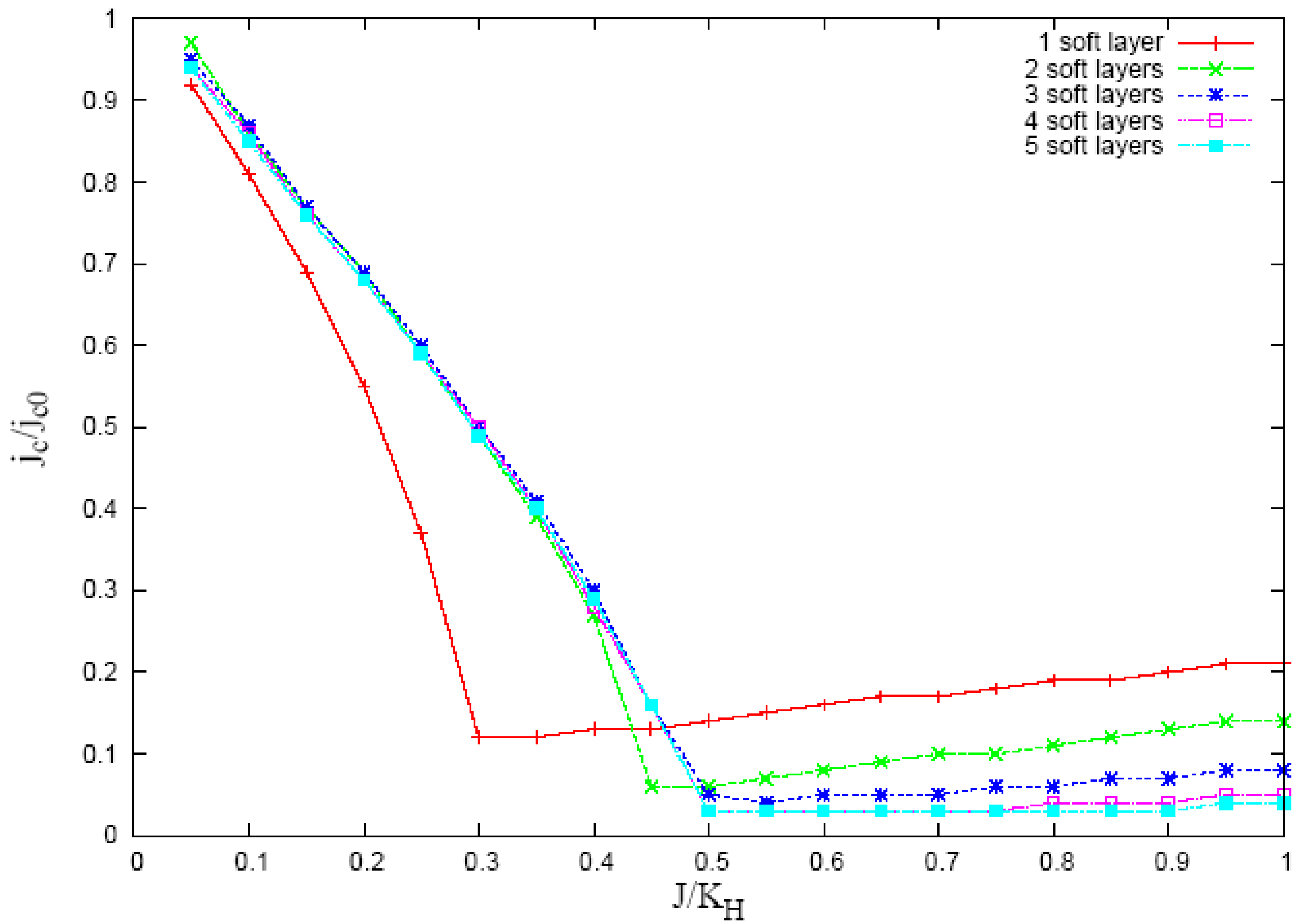

Figure 3.4: The switching current as a function of inter-layer exchange coupling, for different number of assisting layers.

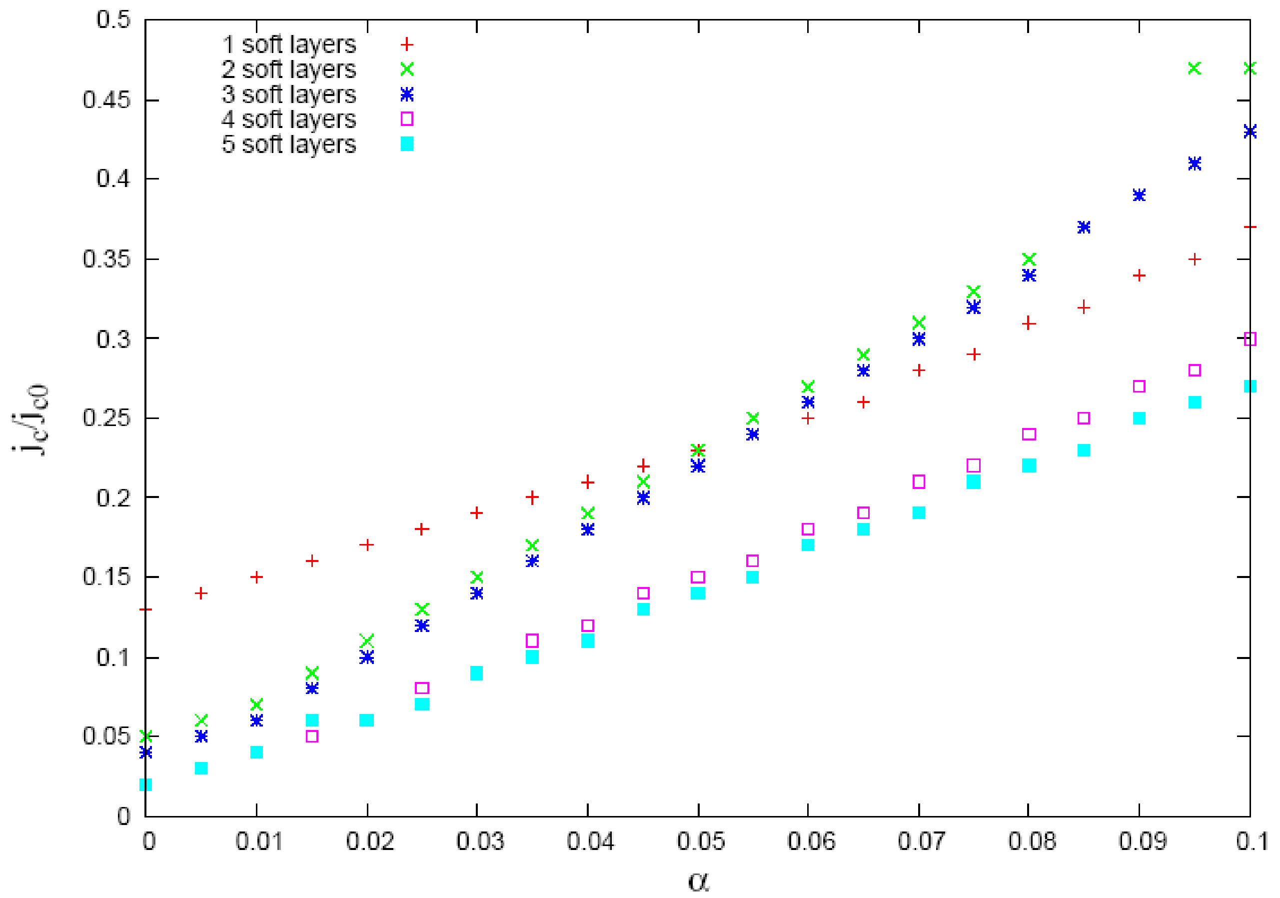

Figure 3.5: The switching current as a function of damping constant in the assisting layers, for different number of assisting layers.

compared to 0.1 in the hard layer. Since the switching current for a single layer is proportional to its damping, it is interesting to see how damping in the soft layer influences the overall switching current. In Fig. 3.5, j_c is calculated as a function of α_S for different number of soft layers. In all cases, j_c increases linearly with α_S. Therefore, to achieve maximal reduction of j_c, low damping in the soft layers is crucial. This is likely to be a realistic goal, since both anisotropy and damping have a major contribution from the spin-orbit interaction and it is reasonable to expect that softer material comes with a lower damping.

3.3 Conclusions

In this chapter, we propose a method to reduce switching current in MTJ. It is shown that by coupling a soft magnetic layer with relatively low damping to a hard magnetic layer, the switching current can be greatly reduced. The reduction mechanism is based on switching the softer layer first and this layer, through exchange coupling, will switch the hard layer. We also show that with multiple soft layers and graded anisotropies, the switching current can be further reduced, by well over an order of magnitude. It is crucial to have low damping in the soft layers and the switching current grows linearly with the increase of damping.

Chapter 4

Phase locking of spin torque oscillators

4.1 Introduction

Steady precessional dynamics of magnetization can be induced by current when the STT exactly cancels the damping torque. The precession of magnetization gives rise to an oscillating electric signal through the magnetoresistive effect, which can be detected experimentally [16]. Due to the nonlinear nature of the magnetization dynamics, the signal frequency depends on the oscillation amplitude, which can be tuned by current [16, 67]. From a technological point of view, this effect is extremely attractive because it offers the possibility of making a microwave oscillator at the nanoscale with frequency tunability.

Recent experiments [3, 68] in point contact geometry have demonstrated that two STOs can be synchronized and oscillate with the same phase. The synchronization of STOs is desireable because it boosts the power output of the device, which is crucial for applications. As in all synchronization phenomena, a coupling mechanism is needed for phase locking. In the experiments, the STOs are not in direct contact with each other and, therefore, they cannot interact through direct exchange coupling. Other possibilities include dipole-dipole interaction and spin wave induced coupling. In an elegant experiment [25], the magnetic film hosting the STOs is cut, thus effectively blocking the path of spinwave propogation between the STOs. After the cut, the phase locking disappears even though dipole-dipole interaction is still present. The experiment provides convincing evidence that spinwave induced coupling is the main mechanism for STO synchronization.

Despite the intensive experimental efforts, the physics of spin wave induced phase lock between STOs is still not fully understood. From a theoretical perspective, simplified models [69, 70] based on coupled non-linear oscillators are proposed to describe the synchronization between STOs and provide an intuitive picture of the nature of the effect. In these simplified models, however, the spatial inhomogeneity of the SW is not taken into account explicitly. Instead, a phenomenological parameter is introduced to describe the coupling, whose physical meaning is yet to be clarified. On the other hand, a micromagnetic simulation has been carried out by Sano [71], in an attempt to elucidate the coupling mechanism beyond a model study. This more

microscopic approach may provide a more detailed understanding. But in Sano's work, the cell size ($70 \times 70\text{nm}^2$) used is so large compared to the SW wavelength that the dynamics of spatially non-uniform ($k \neq 0$) SW modes is missed.

In this chapter, I will discuss my theoretical effort to understand the phase locking of STOs. The approach is to start from the microscopic description of the system, based on micromagnetics. In this way, the spin wave dynamics are fully captured. Based on the microscopic description, I derive an analytic model that is comparable to earlier studies [69, 70] yet contains some new physics, namely the coupling exhibits an oscillatory behavior due to the interference of spin waves. Then, micromagnetic simulation is carried out, using a cell size that is adequately small (2nm) to capture SW excitations. The analytical study is confirmed by numerical calculation.

4.2 Analytical theory

The model geometry used here is similar to experiment [68]. The structure contains two magnetic films, i.e. free and polarization layers, separated by a non-magnetic spacer. The free layer is electrically connected to the electrode through two point contacts. The bottom polarization layer serves as the polarizer for the electric current. An external magnetic field is applied perpendicular to the film plane. In the calculation, we are only concerned with the dynamics of the free layer while assuming the magnetization in the polarizing layer is fixed.

The dynamics is described using the Landau-Lifshitz-Gilbert (LLG) equation with

spin torque term included [18]:

$$\frac{\partial \hat{m}(x)}{\partial t} = -\gamma \hat{m} \times \vec{H}_{eff}(x) + \alpha \hat{m} \times \frac{\partial \hat{m}}{\partial t} + \gamma H_{ST}(x) \hat{m} \times (\hat{m} \times \hat{p}), \tag{4.1}$$

where $\hat{m}(x)$ is the directional vector of local magnetization, γ is the gyromagnetic ratio, α is the damping constant, $\hat{p}$ is the current polarization direction, $H_{ST}(x) = \frac{P\hbar j(x)}{edM_S}$ is the field induced by the spin current j, with thickness of free layer $d = 5$nm and polarization factor $P = 0.25$. Permalloy $Ni_{80}Fe_{20}$ is used as the free layer with standard parameters $M_S = 860$ emu/cm^3, $\alpha = 0.02$ and exchange coupling $A = 10^{-6}$erg/cm.

Defining $m^{\pm} = m_x \pm i m_y$ and $H^{\pm}_{eff} = H_{eff_x} \pm i H_{eff_y}$, we can rewrite [72] the LLG equation Eq. 4.1 as:

$$i\frac{\partial m^+(x)}{\partial t} = \gamma m_z H^+_{eff} - \gamma H_{eff_z} m^+ + i\gamma H_{ST} m_z m^+ + \alpha(\dot{m}_z m^+ - m_z \dot{m}^+) \tag{4.2}$$

The magnetic free energy takes the form: $E = \int (-M_S H_{ex} \cdot m_z(\vec{x}) - 2\pi(m_x^2(\vec{x}) + m_y^2(\vec{x}))M_S^2 + A\left|\nabla \hat{m}(\vec{x})\right|^2] d\vec{x}$.

The effective field $\vec{H}_{eff} = (H_{ex} - 4\pi M_S m_z)\hat{z} + 2\frac{A}{M_S}\nabla^2 \hat{m}$ contains the out of plane external, demagnetization and exchange fields.

Before considering the phase-locking of double point contacts, we first study the case of a single contact in order to validate our model by reproducing established experimental results. For small amplitude oscillation with weak current, $m_z \approx 1$ and Eq. 4.2 can be linearized:

$$\omega u = \frac{\gamma}{1 - i\alpha}(H_{ex} - 4\pi M_S - \frac{2A}{M_S}\nabla^2 - iH_{ST})u, \tag{4.3}$$

where we assumed $m^+(x) = u(x)e^{i\omega t}$. One can solve Eq. 4.3 and obtain the propagating spin wave solution $u(r) = cH_0^{(2)}(kr)$ [73], where k is the wave number, $H_0^{(2)}(x)$ is the Hankel function, and c is a constant to be determined.

When two point contacts are placed on the same film, they interact through the propagating SWs emitted from each other. The total energy can be expressed in terms of the superposition of the spin waves (m_1 and m_2) generated by two contacts, $E = \int [-M_S H_{ex} \cdot (m_{1z} + m_{2z}) + A\,|\nabla(\hat{m}_1 + \hat{m}_2)|^2 - 2\pi[(m_{1x}+m_{2x})^2 + (m_{1y}+m_{2y})^2]M_S^2] d\vec{x}$. Therefore, the equation of motion for each STO is modified from Eq. 4.3:

$$\begin{aligned} -i\dot{m}_1^+ &= \omega_1 m_1^+ - (\tfrac{\gamma}{1-i\alpha}H_{ex} - \omega_2)m_2^+ \\ -i\dot{m}_2^+ &= \omega_2 m_2^+ - (\tfrac{\gamma}{1-i\alpha}H_{ex} - \omega_1)m_1^+ \end{aligned} \tag{4.4}$$

m_n^+ is assumed to follow the form of $m_n^+ = u_n(r)e^{i\phi_n}$ $(n = 1, 2)$. Rewriting Eq. 4.4 in terms of ϕ_n and subtracting the two equations, we obtain the equation of motion for the phase difference:

$$\Delta\dot{\phi} = \Delta\omega - K\sqrt{1 + (\tfrac{\Delta K}{K})^2}\sin(\Delta\phi + \delta), \tag{4.5}$$

where $\Delta\phi = \phi_2 - \phi_1$, $\Delta\omega = \omega_2 - \omega_1$, $K = \mathrm{Im}(f_2 + f_1)$, $\Delta K = \mathrm{Re}(f_2 - f_1)$ and $\delta = \arctan(\frac{\Delta K}{K})$ with $f_1 = (\frac{\gamma}{1-i\alpha}H_{ex} - \omega_2)u_2(\mathbf{R_1})/u_1(\mathbf{R_1})$ and $f_2 = (\frac{\gamma}{1-i\alpha}H_{ex} - \omega_1)u_1(\mathbf{R_2})/u_2(\mathbf{R_2})$. Using the solutions in [73], one can show that $f_1 \propto cH_0^{(2)}(k_1 R_{12}) \overset{k_1 R_{12} >> 1}{\rightarrow} cR_{12}^{-1/2}e^{-ik_1 R_{12}}$ and, similarly, $f_2 \overset{k_2 R_{12} >> 1}{\rightarrow} cR_{12}^{-1/2}e^{-ik_2 R_{12}}$, where $\mathbf{R_n}$, ω_n, and k_n are the location, frequency, and wave number for STO n $(n = 1, 2)$. Therefore, K will exhibit sinusoidal oscillation as a function of separation between contacts R_{12}. Note that Eq. 4.5, known as Adler's equation [74], is a general

description for synchronization arising in various contexts such as electric circuits, Josephson junctions [75] *etc.*

An important prediction of Eq. 4.5 is that as we vary R_{12}, the two STOs will alternatively exhibit in phase, i.e. $\Delta\phi \approx 0$ for positive K, and out of phase oscillation, i.e. $\Delta\phi \approx \pi$ for negative K, with the period being the SW wavelength. This is manifested through the microwave power emitted from the sample. With in phase oscillation, the wave emitted from the two STOs is added constructively, while in the out of phase case, they cancel each other leading to a vanishing emission power. Additionally, in the usual case of two phase-locked similar oscillators, ΔK will be small, $\Delta\dot{\phi} = 0$, and therefore

$$\sin \Delta\phi \approx \frac{\Delta\omega}{K} \tag{4.6}$$

4.3 Micromagnetic simulation

In this section micromagnetic simulation is performed. As mentioned in the introduction, a sufficiently small grid size is required to capture the spin waves. Here it is chosen to be $2nm$, much smaller than the spin wavelength which is about $30nm$. In experiment, the film size is several micrometers, which is larger than other characteristic length scales in the system, and can be regarded as infinite. However, in numerical calculation, the sample size is limited which introduces an artificial boundary effect. In particular, spin wave reflection off the boundary causes chaotic behavior of the system. To avoid this problem, a large damping constant is imposed on the

boundary, so that the spin waves are absorbed, as suggested by Berkov et al. [76].

To compare with experiment and visualize the SW solution $u(r)$, we solve the LLG equation with a single contact numerically. The micromagnetic simulation scheme follows Dobin and Victora [77], with the addition of a spin torque term described in Eq. 4.1. The precession frequency is determined by the effective field perpendicular to the film plane. On the other hand, the z component of the demagnetization field can be tuned by the current density. Therefore frequency-tunability can be realized by varying the current. Fig. 4.1(a) shows the peak frequency's dependence on current as compared to the experiment[4], where the contact diameter is $36nm$ and a perpendicular external field $H_{ex} = 1T$ is applied. We also calculated other experimental diameters and similar agreements are found. Both the experiment and calculation shows a linear relation between current and frequency. The steady-state SW configuration excited by the point contact is shown in Fig. 4.1(b).

Experiments [3, 68] have shown that there exists a phase-lock regime where two STOs with slightly different intrinsic frequencies synchronize. We first carry out simulation to reproduce the experimental observation. In the calculation, we place two contacts, with diameters 20nm, 500nm apart on a $704 \times 704\text{nm}^2$ sample, with a perpendicular external field $1.5T$. The current through one contact is fixed at $I_1 = 4.5$mA and I_2 is varied from 4.1mA to 5mA. The power spectrum density (PSD), which is calculated from the square of the Fourier transform of the overall magnetization, as a function of I_2 is plotted in Fig. 4.2(a). Similar to experiment [3,

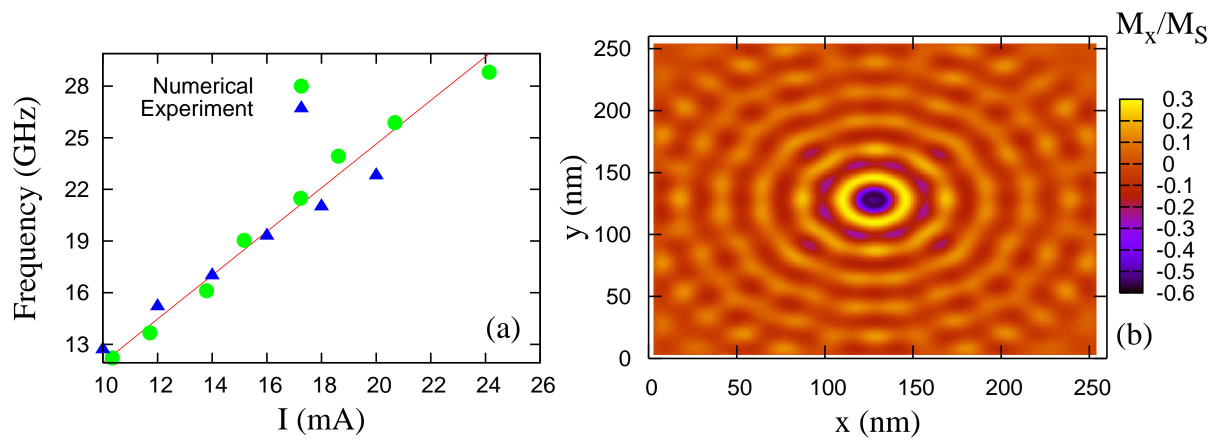

Figure 4.1: (a) Calculated dependence of peak frequency on wire width (circles) with a linear fit (solid line) and experimental results extracted from [4]. (b) a snap-shot of the steady state SW configuration generated by the point contact.

68], there exists a phase-locked region (4.3mA < I_2 < 4.7mA) in which the spectrum shows a single peak and the intensity is large. Outside this range, two distinct peaks are present and the power is significantly weaker. In particular, the spectrum for $I_2 =$ 4.6mA is shown in Fig. 4.2(b) within the phase-locked region, while for $I_2 = 5.0$mA (Fig. 4.2(c)) two separate peaks are present indicating the absence of phase-locking. It is also noticeable that the calculated results are quantitatively different from those observed in experiment [3]. In the present calculation, the two contacts are identical while, in experiment, the two ostensibly similar oscillators behave differently outside the phase lock regime.

To confirm the prediction of oscillatory coupling between STOs, we vary the distance R_{12} with $I_1 = 4.5$mA and $I_2 = 1.04I_1$. The two STOs are placed on the film symmetrically (for example, see Fig. 4.4(d)). The combined PSD is shown in Fig. 4.3 as a function of frequency and distance from 60nm to 220nm. Though $I_1 \neq I_2$, the two STOs are phase-locked through out the whole range. The power oscillates with R_{12} with a period of about 34nm, which agrees with the SW wavelength estimated from the dispersion relation.

In Figs. 4.4(a) and (b), we show the stationary phase difference $\sin \Delta\phi$ versus frequency difference $\Delta\omega$. Experimentally, $\Delta\phi$ can be measured by varying the phase between signals from two contacts using a phase shifter and observing the sinusoidal variation of the output power, as demonstrated in [3]. The linear relation observed in 4.4 is consistent with Eq. 4.6 and the slope is the inverse coupling parameter $1/K$.

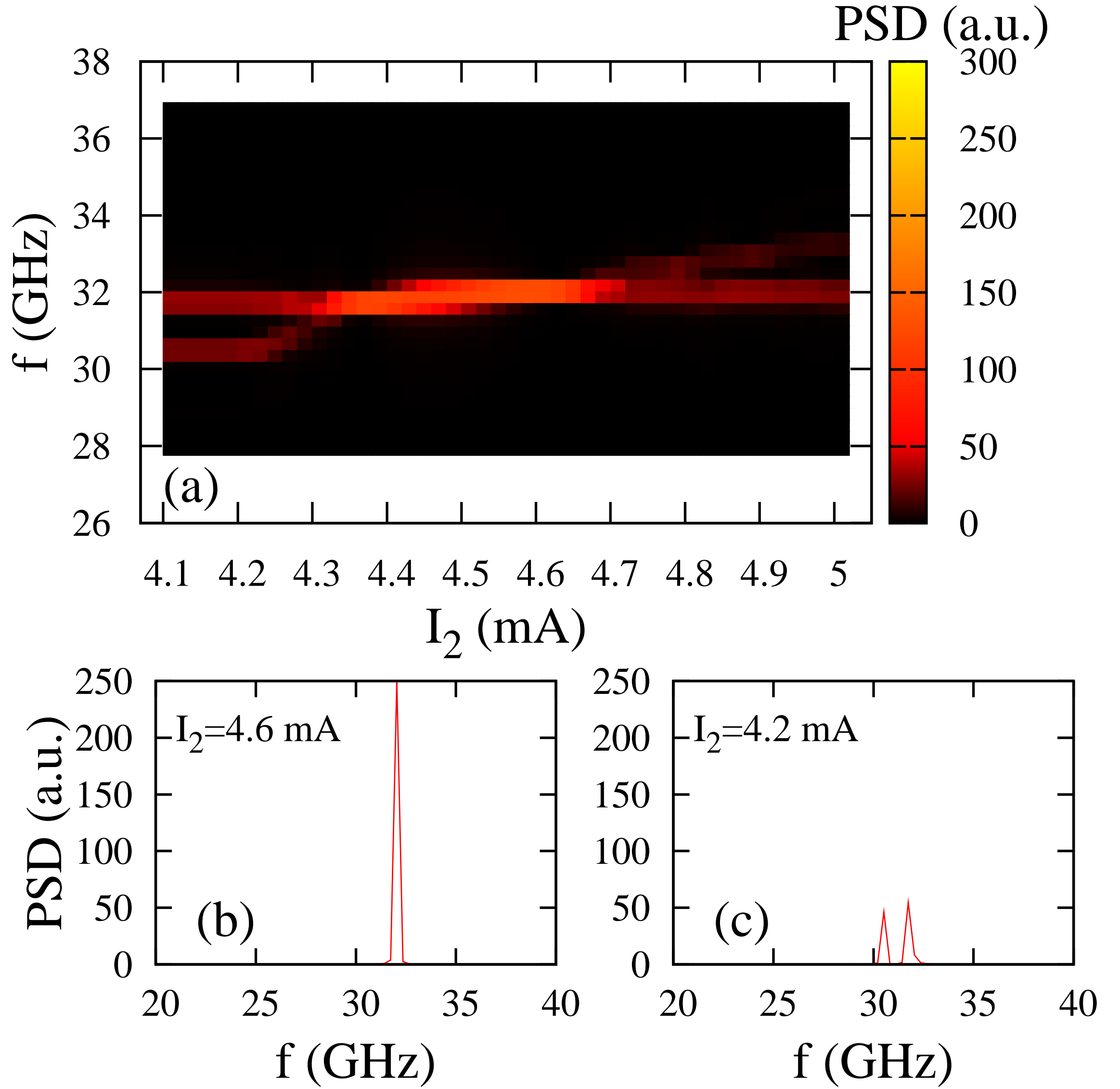

Figure 4.2: Phase-lock of two STOs spaced at 500 nm. The current of one contact is fixed at $I_1 = 4.5$mA, while I_2 is varied. (a) The map of PSD versus the frequency and I_2. (b) For $I_2 = 4.6$mA, the two contacts are phase-locked with a single peak and significantly larger output power. (c) For $I_2 = 4.2$mA, the two contacts are not phase-locked and two distinct peaks are shown.

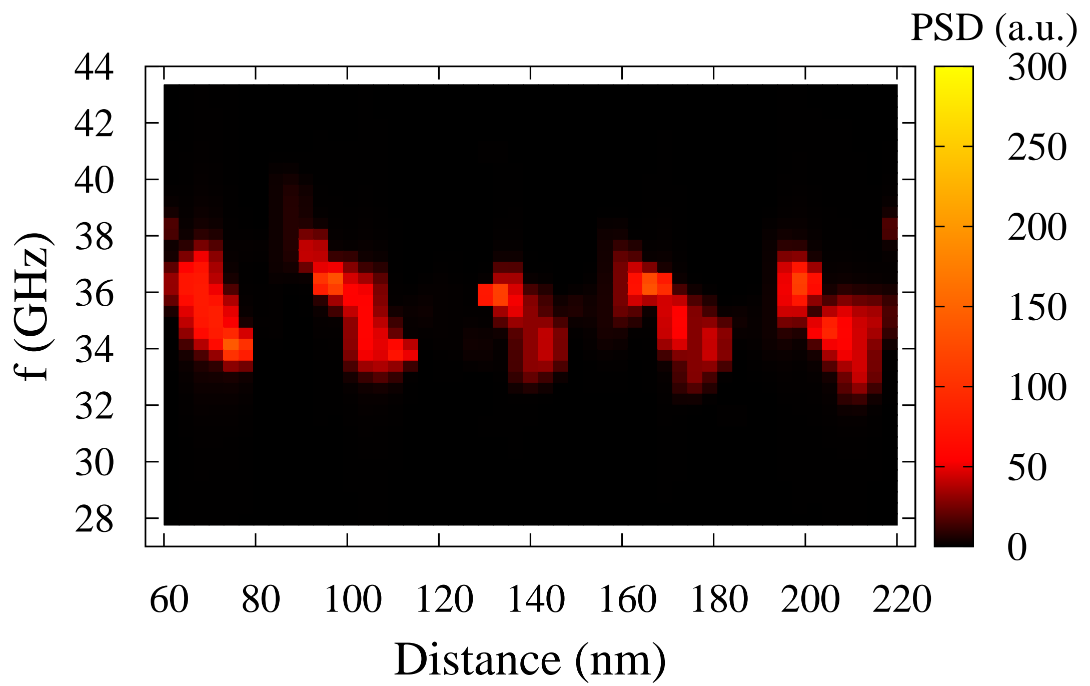

Figure 4.3: The map of the combined power spectrum from both contacts versus frequency and distance R_{12}. The oscillation of output signal is caused by the oscillating coupling parameter $K(R_{12})$. The period is about 34nm that matches the estimated SW wavelength.

When $R_{12} = 100$nm, the slope is positive leading to a positive K. In Fig. 4.4 (b), the slope is reversed indicating a negative K at $R_{12} = 188$nm. The SW configurations for these two cases are shown in Fig. 4.4(c) and (d). Furthermore, we calculate the coupling parameter K as a function of distance R_{12}. The results are plotted along with the analytic expression of K as previously defined in Fig. 4.4(e). The good agreement between simulation and theory in Fig. 4.4(e) demonstrates the validity of the effective equation of motion Eq. 4.5.

In order to detect the oscillating behavior of the coupling parameter, instead of varying R_{12}, one can alternatively fix R_{12} and vary k or the SW wavelength. Notice that the STO allows one to tune the frequency by changing the current and from the SW dispersion relation $\omega = \gamma H_z(k) + \frac{\gamma A}{M_S} k^2$ [73], wavelength tuning can also be realized. Therefore one can change the coupling parameter as well as the output power by varying the current. This effect is displayed in Fig. 4.5 (b), where the integrated power varies dramatically with current I while keeping $I = I_1 = I_2$ and $R_{12} = 200$nm. A similar dependence of power on current is observed in [68]. Additionally, the blue shift of peak frequency is shown in Fig. 4.5 (a).

In the present calculations, the Oersted field produced by the current is neglected to simplify the theoretical analysis. However, we have done calculations including the Oersted field and no qualitative difference is found. Hoefer [78] has shown that application of an applied field at an angle to the surface normal can, in combination with the Oersted field, direct the spin waves so that one spin torque oscillator receives

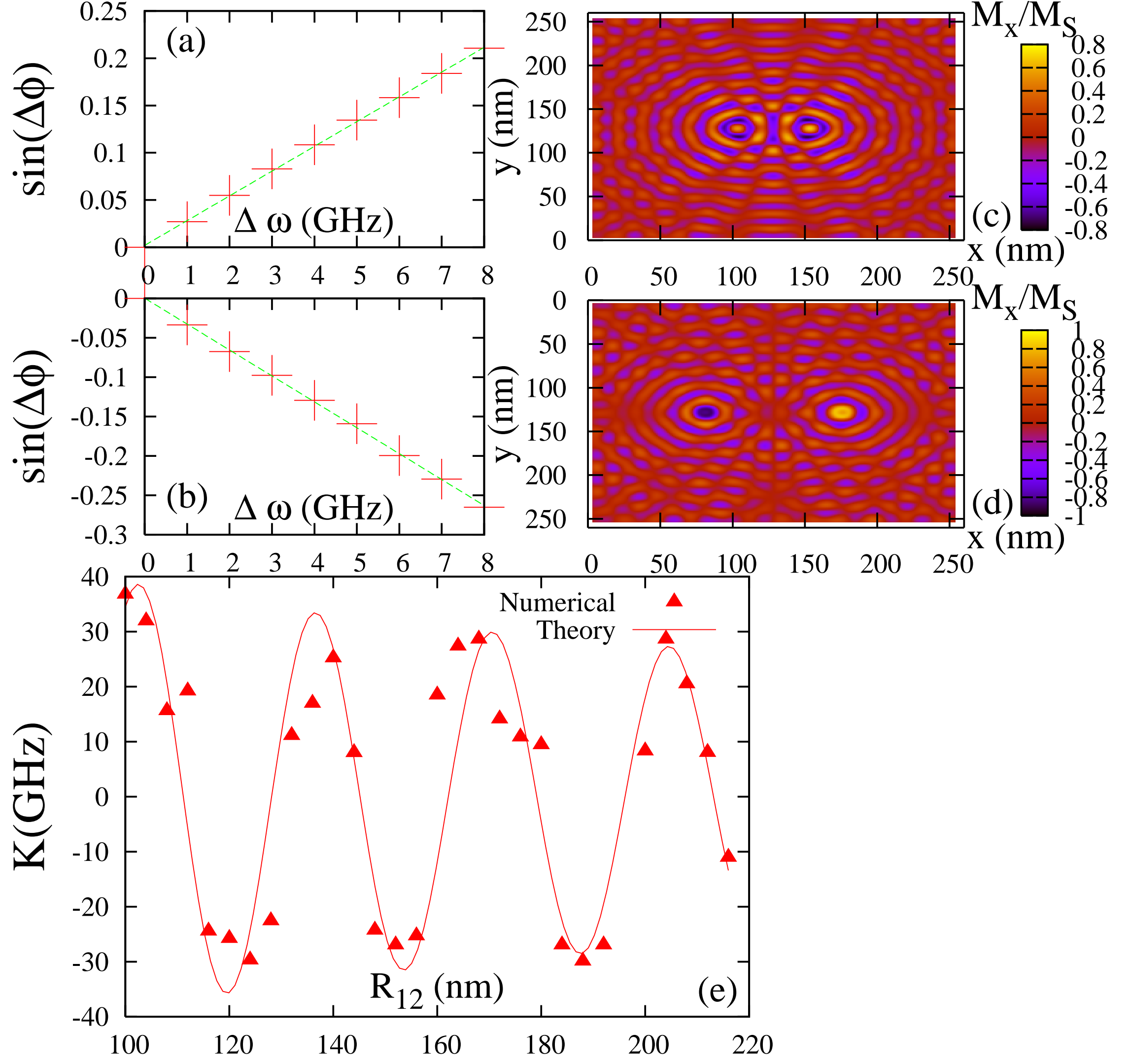

Figure 4.4: Calculated dependence of phase difference on frequency difference using Eq. 4.6 (line) and simulation (+) for R_{12} = 100nm (a) and R_{12} = 188nm (b). Snapshot of the respective SW configuration shown in (c) and (d). (e) shows the coupling parameter $K(R_{12})$ from simulation using and theoretically evaluated using $K(R_{12}) = \text{Im}[(\frac{\gamma}{1-i\alpha}H_{ex} - \omega_1)cH_0^{(2)}(k_1R_{12}) + (\frac{\gamma}{1-i\alpha}H_{ex} - \omega_2)cH_0^{(2)}(k_2R_{12})]$.

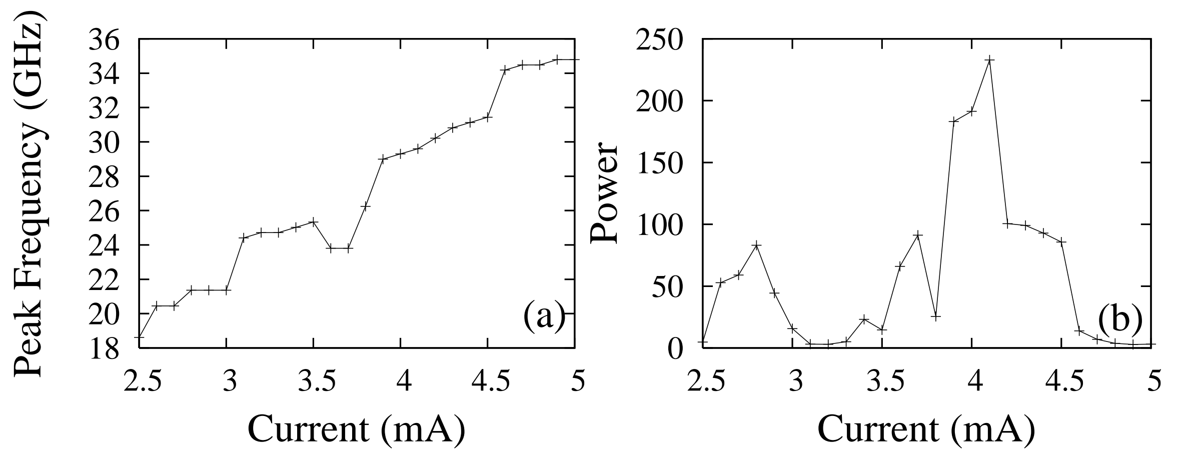

Figure 4.5: Simultaneous variation of currents under both contacts while keeping $I_1 = I_2$. (a) The blue shift of peak frequency with increasing current. (b) The variation of the integrated power.

a reduced number from the other. Our calculations show, however, that this second spin torque oscillator will, in turn, radiate an increased number towards the first one and thus our principle of coupling spin torque oscillators through spin waves is preserved.

Another factor that affects the phase locking is the surface profile of the contact. The contact is not a point like object and one can not define a unique distance between two contacts. On the other hand, the coupling strength is sensitive to the distance. For a rough contact, the distance between two points on the contact fluctuates randomly, therefore the coupling is averaged over a range determined by the roughness. In particular, when the roughness of the contact surface is comparable to the SW wavelength, our calculations show that the line width becomes wider and the coupling strength is weakened.

4.4 Conclusions

In this chapter, we presented an analytical theory of the phase locking between STOs in a point contact geometry. We identified the spin-wave as the mechanism for the coupling and derived an explicit expression for the coupling parameter.

The coupling parameter exhibits an oscillatory behavior versus the contact separation R_{12}, with the period equaling the spin-wave wavelength. As a consequence, the STOs will alternate between in-phase and out-of-phase oscillation, corresponding to maximal and minimal output power. This has significant impact on the performance

of the STO devices.

Micromagnetic simulation is carried out and confirms the predicted behavior. The analytic expression for coupling parameter is found to agree well with the numerical values. We calculated the power spectrum of the coupled STO system as a function of current and distance. We also proposed an experiment that detects the effect by varying the current.

Bibliography

[1] J.Barnas *et al.*, Phys. Rev. B **42**, 8110 (1990).

[2] P. Braganca *et al.*, Appl. Phys. Lett. **87**, 112507 (2005).

[3] S. Kaka, M. R. Pufall, W. H. Rippard, T. J. Silva, S. E. Russek, and J. A. Katine, Nature (London) **437**, 389 (2005).

[4] F. B. Mancoff, N. D. Rizzo, B. N. Engel, and S. Tehrani, Appl. Phys. Lett. **88**, 112507 (2006).

[5] N. W. Ashcroft and N. D. Mermin, *The Solid State Physics* (Brooks Cole, 1976).

[6] R. C. O'Handley, *The Modern Magnetic Materials: Principles and Applications* (Wiley-Interscience, 1999).

[7] M. N. Baibich *et al.*, Phys. Rev. Lett. **61**, 2472 (1988).

[8] G. Binasch *et al.*, Phys. Rev. B **39**, 4828 (1989).

[9] J. S. Moodera *et al.*, Phys. Rev. Lett. **74**, 3273 (1995).

[10] T. Miyazaki *et al.*, J. Magn. Magn. Mater. **139**, L231 (1995).

[11] W. H. Butler *et al.*, Phys. Rev. B **63**, 054416 (2001).

[12] L. Berger, Phys. Rev. B **54**, 9353 (1996).

[13] J. C. Slonczewski, J. Magn. Magn. Mater. **159**, L1 (1996).

[14] E. B. Myers *et al.*, Science **285**, 867 (1999).

[15] J. A. Katine *et al.*, Phys. Rev. Lett. **84**, 3149 (2000).

[16] S. I. Kiselev, J. C. Sankey, I. N. Krivorotov, N. C. Emley, R. J. Schoelkopf, R. A. Buhrman, and D. C. Ralph, Nature (London) **425**, 380 (2003).

[17] A. Yamaguchi *et al.*, Phys. Rev. Lett. **92**, 077205 (2004).

[18] S. Zhang and Z. Li, Phys. Rev. Lett. **93**, 127204 (2004).

[19] J. Wang *et al.*, Appl. Phys. Lett. **87**, 043101 (2005).

[20] L. Jiang *et al.*, Appl. Phys. Express **2**, 083002 (2009).

[21] P. X. Xu *et al.*, Phys. Rev. B **73**, 180402 (2006).

[22] D. C. Ralph and M. D. Stiles, J. Magn. Magn. Mater. **320**, 1190 (2008).

[23] G. D. Fuchs *et al.*, Appl. Phys. Lett. **85**, 1205 (2004).

[24] D. Houssameddine *et al.*, Nat. Materi. **6**, 447 (2007).

[25] M. R. Pufall, W. H. Rippard, S. E. Russek, S. Kaka, and J. A. Katine, Phys. Rev. Lett. **97**, 087206 (2006).

[26] J. Grollier *et al.*, Phys. Rev. B **73**, 060409 (2006).

[27] W. H. Rippard *et al.*, Phys. Rev. Lett. **92**, 027201 (2004).

[28] R. Landauer, Philos. Mag. **21**, 863 (1970).

[29] S. Datta, *Electronic Transport in Mesoscopic Systems* (Cambridge University Press, Cambridge, 1997).

[30] Z.-S. Zhang and D. A. Rabson, J. Appl. Phys. **95**, 557 (2004).

[31] V. D. Costa *et al.*, Phys. Rev. Lett. **85**, 876 (2000).

[32] B. J. Jonsson-Akerman *et al.*, Appl. Phys. Lett. **77**, 1870 (2000).

[33] P. Bruno, Phys. Rev. Lett. **83**, 2425 (1999).

[34] J. S. Moodera *et al.*, Phys. Rev. Lett. **80**, 2941 (1998a).

[35] A. R. Rocha and S. Sanvito, J. Appl. Phys. **101**, 09B102 (2007).

[36] S. Zhang *et al.*, Phys. Rev. Lett. **79**, 3744 (1997).

[37] S. Mukhopadhyay and I. Das, Phys. Rev. Lett. **96**, 026601 (2006).

[38] D. A. Rabson *et al.*, J. Appl. Phys. **89**, 2786 (2001).

[39] T. Dimopoulos *et al.*, J. Appl. Phys. **89**, 7371 (2001).

[40] H. Fukuzawa *et al.*, J. Phys. D: Appl. Phys. **40**, 1213 (2007).

[41] C. A. Foss *et al.*, Adv. Mater. **5**, 135 (1993).

[42] J. Rivas *et al.*, J. Magn. Magn. Mater. **249**, 220 (2002).

[43] L. Piraux *et al.*, Appl. Phys. Lett. **65**, 2484 (1994).

[44] A. Blondel *et al.*, Appl. Phys. Lett. **65**, 3019 (1994).

[45] X. Duan, Y. Huang, Y. Cui, J. Wang, and C. M. Lieber, Nature (London) **409**, 66 (2001).

[46] L. Dong *et al.*, Nano Lett **5**, 2112 (2005).

[47] E. Sondheimer, Adv. Phys. **1**, 1 (1952).

[48] A. Mayadas and M. Shatzkes, Phys. Rev. B **1**, 1382 (1970).

[49] C. Durkan and M. E. Welland, Phys. Rev. B **61**, 14215 (2000).

[50] W. Steinhogl *et al.*, Phys. Rev. B **66**, 075414 (2002).

[51] Y. Wu *et al.*, Nature (London) **430**, 61 (2004).

[52] M. E. T. Molares *et al.*, Appl. Phys. Lett. **82**, 2139 (2003).

[53] J. Li *et al.*, J. Appl. Phys. **70**, 2820 (1991).

[54] J. S. Moodera *et al.*, Phys. Rev. Lett. **80**, 2941 (1998b).

[55] M. Büttiker, Phys. Rev. Lett. **57**, 1761 (1986).

[56] D. K. Ferry and S. M. Goodnick, *Transport in Nanostructures* (Cambridge University Press, Cambridge, 1997).

[57] T. N. Todorov, Phys. Rev. B **54**, 5801 (1996).

[58] P. W. Anderson, Phys. Rev. **109**, 1492 (1958).

[59] D. J. Thouless, Phys. Rev. Lett. **39**, 1167 (1977).

[60] B. L. Altshuler, D. Khmel'nitzkii, A. I. Larkin, and P. A. Lee, Phys. Rev. B **22**, 5142 (1980).

[61] B. S. Chun *et al.*, Journal of Magnetism and Magnetic Materials **272-276**, e1481 (2004).

[62] K. Tsunekawa *et al.*, Appl. Phys. Lett. **87**, 072503 (2005).

[63] L. Tan *et al.*, J. Appl. Phys. **103**, 07B504 (2008).

[64] Y. Huai *et al.*, Jpn. J. Appl. Phys. **45**, 3835 (2006).

[65] H. Meng and J.-P. Wang, Appl. Phys. Lett. **89**, 152509 (2006).

[66] R. H. Victora and X. Shen, IEEE Transactions on Magnetics **41**, 2828 (2005).

[67] T. J. Silva and W. H. Rippard, J. Magn. Magn. Mater. **320**, 1260 (2007).

[68] F. B. Mancoff, N. D. Rizzo, B. N. Engel, and S. Tehrani, Nature (London) **437**, 393 (2005).

[69] S. M. Rezende, F. M. de Aguiar, R. L. Rodrguez-Surez, and A. Azevedo, Phys. Rev. Lett. **98**, 087202 (2007).

[70] A. N. Slavin and V. S. Tiberkevich, Phys. Rev. B **74**, 104401 (2006).

[71] E. Sano, Japanese Journal of Applied Physics **46**, L1123 (2007).

[72] M. A. Hoefer, M. J. Ablowitz, B. Ilan, M. R. Pufall, and T. J. Silva, Phys. Rev. Lett. **95**, 267206 (2005).

[73] J. C. Slonczewski, J. Magn. Magn. Mater. **195**, L261 (1999).

[74] R. Adler, Proc. IEEE **61**, 1380 (1973).

[75] K. Wiesenfeld, P. Colet, and S. H. Strogatz, Phys. Rev. Lett. **76**, 404 (1996).

[76] D. Berkov and J. Miltat, J. Magn. Magn. Mater. **320**, 1238 (2008).

[77] A. Y. Dobin and R. H. Victora, Phys. Rev. Lett. **90**, 167203 (2003).

[78] M. A. Hoefer, T. J. Silva, and M. D. Stiles, Phys. Rev. B **77**, 144401 (2008).